Geophys. J. Int. (1996) **124,** 502–524

A model for sedimentary compaction of a viscous medium and its application to inner-core growth

Ikuro Sumita,[1] Shigeo Yoshida,[2] Mineo Kumazawa[3] and Yozo Hamano[1]

[1]*Department of Earth and Planetary Physics, Faculty of Science, University of Tokyo, Tokyo* 113, *Japan*
[2]*Earthquake Research Institute, University of Tokyo, Tokyo* 113, *Japan*
[3]*Department of Earth and Planetary Science, Faculty of Science, Nagoya University, Nagoya* 464-01, *Japan*

Accepted 1995 August 30. Received 1995 April 26; in original form 1994 September 27

SUMMARY

A detailed study of the physics of a 1-D sedimentary compaction of a viscous medium was carried out both numerically and analytically for columnar and self-gravitating spherical cases, in view of applying it to the inner-core growth process of the Earth. The effects of sedimentation rate and surface porosity upon the porosity profile were investigated. It was found that the porosity profile differs depending on whether or not the sedimentation rate is larger than the Darcy velocity (velocity of the solid matrix when the fluid flows by buoyancy alone). When the sedimentation rate is larger than the Darcy velocity, a thick, constant-porosity layer develops at the surface, and below it, the porosity decreases gradually towards the bottom. When the sedimentation rate is smaller than the Darcy velocity, the porosity profile is characterized by a mushy layer at the top, where the fluid is expelled by the deformation of the solid, underlain by a thick layer of constant porosity, termed the residual porosity. Such a porosity profile can be understood as the propagation of a half-sided solitary wave. The study was extended further for the self-gravitating spherical case. Formation of an unstable porosity structure and the appearance of solitary waves were discovered for the case of monotonically decreasing sedimentation rate. Given the size of the sphere formed by sedimentary compaction, according to the magnitude of the ratio of sedimentation rate to Darcy velocity, three types of porosity structure, which differ in force balance and the typical length scale required for porosity decrease, were discovered. One such structure is where a low-porosity layer forms at the top, accompanied by solitary waves beneath it, indicating that a crust-like region can develop at the surface of the inner core.

Key words: inner core, permeability, porosity, sedimentation.

1 INTRODUCTION

Sedimentary compaction appears in various fields of the earth sciences. It is a common process that occurs not only in compacting sediments in lakes and on sea floors, but also as densification or age-hardening of snow (Gow & Ramseier 1963), sedimentation of volcanic ash, and as cumulate formation in magma chambers (Irvine 1980; Sparks *et al.* 1985) or magma oceans, the latter of which are considered to have formed during the early stages of the Earth's formation (Safronov 1978).

Another important application is the inner-core growth process, which is believed to have been occurring throughout the Earth's history by cooling of the core (e.g. Jacobs 1953). The formation of a partially molten inner core is an inevitable consequence of the solidification of a liquid iron core that contains impurities (e.g. Birch 1964), as can be seen in dendritic growth of crystals in solidifying alloys, so the inner core can be regarded as the cumulative result of precipitation and sedimentary compaction of solid iron particles.

There have been several works concerning the structure of the inner core. Fearn, Loper & Roberts (1981) and Loper & Fearn (1983) argued that the mushy layer, a layer of partially molten state, may extend to the centre of the Earth from simple thermodynamic considerations by using a phase diagram. Loper (1983) proposed that through compositional freezing by the downward flow of the outer-core fluid into the inner core, the mushy layer becomes thin. We propose that the compaction process of the solid matrix, which has been neglected in the previous studies, is of primary importance to the structure of the inner core, because of the large spatial and temporary scales involved for the inner-core growth.

The objective of this paper is to make a detailed study of the physics of sedimentary compaction from both numerical and analytical aspects, and in columnar and self-gravitating spherical cases using fluid dynamic equations and constitutive

relations, in order to provide the bases of applying it to the inner-core growth process. Our model is simple, but we have shown that when we apply this model to the inner core, even in the presence of other effects such as that of convection, the structure is primarily determined by compaction.

In modelling the dynamics of partial melt it should be borne in mind that there are three types of partially molten states, depending on whether each of the two states, solid and liquid, link together or not. Stevenson (1990) analogously named these as being in the state of the 'meat ball', when only the liquids link together, the 'sponge', when both solid and liquid link together and the 'swiss cheese', when only solids link together. The former two may also be called 'slurry' or 'mush', respectively. We will assume that the inner core is in the state of the 'sponge' or 'mush' domain where the solid forms a matrix (i.e. solid grains link together) and compacts, while the interstitial melt, which is also linked together, seeps out from the matrix as a permeable flow.

The physics of sedimentary compaction has long been investigated in the study of sedimentary basins (e.g. Gibson 1958). In most of these studies, the mechanical behaviour of the compacting solid material has been regarded as plastic and conventionally treated as elastic for mathematical convenience. In recent years, numerical solutions have been obtained for the evolution of porosity (Audet & Fowler 1992) as well as for temperature by considering heat conduction (Wangen 1992). In both of these works, the sedimentation rate dependence on the porosity profile was studied and it was found that the compaction mechanics were governed by the ratio of sedimentation rate to permeability.

The process of compaction was formulated in another way, originating from the study of magma. McKenzie (1984) derived and analysed the governing equations for compaction by treating the compacting solid as a viscous medium. He defined the compaction length as a typical length scale for compaction to occur when a column of partial melt is placed on an impermeable plane. Richter & McKenzie (1984) obtained dynamical solutions for partial melt which was left on an impermeable plane and then applied it to the movement of trace elements (Richter 1986). Ribe (1985) derived time-independent stationary solutions for a compacting partial melt in an ascending magma. He defined the reduced compaction length, which is a typical length scale for compaction when the magnitude of the velocity given as the boundary condition is smaller than the magnitude of the Darcy flow, the flow without compaction occurring. Shirley (1986) solved the sedimentary compaction problem numerically and applied it to igneous cumulates. McKenzie (1987) calculated the result of constant sedimentation of partial melt upon an initially uniform column of partial melt. By making several approximations, Fowler (1990) analysed compaction coupled with heat transfer. In Birchwood & Turcotte (1994), unlike in the previous works on sedimentary basins, the solid was assumed to deform as a viscous medium, and the compaction of an initially present column of solid–liquid composite was investigated.

In this paper we will treat the solid–fluid composite as a Newtonian viscous fluid, similar to that in McKenzie (1984), but we distinguish the pressure of the solid and the fluid following Scott & Stevenson (1986). Verification of the above assumption of rheology is also given in this paper. By assuming viscous flow, we were able to see that the porosity profile could be considered as a propagation of a solitary wave, and also discovered a case where decompaction and formation of solitary waves occurs. Such a property was analysed, as has been done by several authors (Scott & Stevenson 1984; Scott & Stevenson 1986; Barcilon & Richter 1986) for similar equations for the system where a mass of magma ascends through a deformable solid matrix. These phenomena could not be described by treating the solid as plastic.

This paper provides the first thorough numerical and analytical study of the time-evolving, compacting sedimentary system by treating the solid as a viscous medium. The problem was studied not only for the columnar case but also for the self-gravitating spherical case, in view of applying it to the inner core. Our numerically calculated results of the columnar case agree with the study by Shirley (1986), who numerically solved a similar set of equations, but did not fully investigate the porosity profile and its parameter dependences from analytical aspects. In this paper, we have also derived analytical solutions, to confirm and understand the numerically obtained results, and to present explicit parameter dependences of the features that characterize the porosity structure.

The parameters of importance in non-dimensionalized equations are the sedimentation rate and the surface porosity, and we will consider the effects of these upon the porosity profile thus formed in a wide parametric range. When considering dimensionalized solutions, the magnitudes of solid viscosity and permeability become important.

We will treat the problem in Sections 2 to 6 using 1-D Cartesian coordinates, in order to understand the basic physics of the columnar case, and in Section 7 we will consider the sedimentary compaction in a self-gravitating sphere, which is the case for the inner core and in planetary bodies. From Section 2 to Section 4, the governing equations and the choice of constitutive relations are described. In Section 5, we make a numerical study of a columnar sedimentary compaction problem and the effects of parameters upon the porosity profile, which is analytically analysed in Section 6. In Section 7 we study compaction in a self-gravitating sphere and then apply it to the inner-core growth process in Section 8.

2 GOVERNING EQUATIONS

The statement of the problem is as follows. Solid particles of a certain grain size precipitate upon an impermeable plane at a constant sedimentation rate V_0, a partial melt of porosity ϕ_0 forms at the surface, and a column of partial melt grows with time. At the same time, compaction of the solid matrix occurs due to its own weight and the column decreases in height. By solving the time evolution of the sedimentation and compaction, the evolution of the porosity structure and the increase in the height of the column are solved, as shown schematically in Fig. 1. The situation is the same as in Audet & Fowler (1992).

The basic equations governing sedimentary compaction are described below. The z axis is taken as positive upwards, $z=0$ being the base and $z=h$ being the surface of the solid–fluid composite. The equations described below follow the formulation of McKenzie (1984), except that we shall regard the pressure difference between solid and fluid as driving the compaction process, as has been formulated by Scott & Stevenson (1986).

The most common example of sedimentary compaction is the case where the matrix is solid and the fluid is liquid, but there could be other types, such as when the fluid is a gaseous phase, such as in volcanic ashes and snow.

The basic equations are written as the set of conservation

Table 1. Notation.

Variable	Meaning	Dimensions
a	grain size	m
G	gravitational constant	Nm^2kg^{-2}
g	gravitational acceleration	ms^{-2}
H	mushy layer thickness	m
$\dot{h}$	growth rate of the composite system	ms^{-1}
K	constant in permeability	none
K_ϕ	permeability	m^2
L_C	compaction length	m
L_R	reduced compaction length	m
P_f	fluid pressure	Pa
P_s	solid pressure	Pa
ΔP	differential pressure: $P_s - P_f$	Pa
r	radius	m
R_{IC}	inner core radius	m
t	time	s
T_C	compaction time	s
U	total volume flux: $\phi v + (1-\phi)V$	ms^{-1}
V	solid velocity	ms^{-1}
v	liquid velocity	ms^{-1}
V_D	Darcy velocity	ms^{-1}
V_0	sedimentation rate (>0)	ms^{-1}
z	vertical coordinate	m
ζ	Lagrangian vertical coordinate	m
η_s	shear viscosity of solid iron	Pas
η_ϕ^*	effective viscosity of solid	Pas
η_f	shear viscosity of melt	Pas
κ	thermal diffusivity	m^2s^{-1}
μ	solid rigidity	Pa
ϕ	porosity	none
ϕ_0	surface porosity	none
ϕ_r	residual porosity	none
Φ	$-\ln\phi$	none
ψ	solidity (1-porosity)	none
ρ_s	solid density	kgm^{-3}
ρ_f	fluid density	kgm^{-3}
$\Delta\rho$	$\rho_s - \rho_f$	kgm^{-3}

- a circumflex ˆ denote the non-dimensionalized form

equations. Conservation of mass for fluid gives

$$\frac{\partial\phi}{\partial t} + \nabla\cdot(\phi\mathbf{v}) = 0, \tag{1}$$

and for a solid matrix

$$\frac{\partial}{\partial t}(1-\phi) + \nabla\cdot(1-\phi)\mathbf{V} = 0, \tag{2}$$

where ϕ is the porosity, $\mathbf{v}$ is the fluid velocity and $\mathbf{V}$ is the solid velocity. Each one of the two phases is incompressible.

Conservation of momentum can be described by the Darcy's law for fluid,

$$\phi(\mathbf{v}-\mathbf{V}) = -\frac{K_\phi}{\eta_f}(\nabla P_f - \rho_f\mathbf{g}), \tag{3}$$

and by hydrostatic approximation for the total solid matrix and the fluid,

$$\nabla\{(1-\phi)P_s + \phi P_f\} = \{(1-\phi)\rho_s + \phi\rho_f\}\mathbf{g}, \tag{4}$$

where K_ϕ is the permeability as a function of porosity under given grain size, η_f is the fluid viscosity, and P_s and P_f are the solid and fluid pressures, respectively. We have assumed hydrostatic approximation because the compaction is assumed to progress slowly and hence we can safely neglect the inertial term.

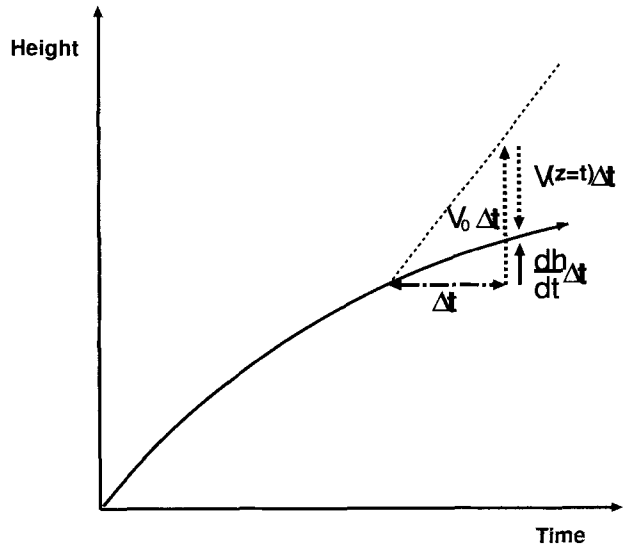

Figure 1. A diagram illustrating the setting for sedimentary compaction. The column of the solid–liquid composite grows as the solid particles precipitate at the sedimentation rate of V_0, but the compaction V causes the actual growth rate $\dot{h}$ to become smaller. The resulting evolution of the trajectory of the surface is calculated.

The compaction of the matrix occurs by differential pressure, i.e. the pressure difference between solid and fluid,

$$\Delta P \equiv P_s - P_f = -\eta_\phi^*\nabla\cdot\mathbf{V}, \tag{5}$$

where η_ϕ^* is the effective bulk viscosity of the matrix as a function of porosity. We have assumed the matrix to behave as a viscous fluid, as opposed to the often-assumed elastic or plastic deformation in the study of sedimentary basins. This is because for the time scale of the inner core growth of $\sim 10^{16}$ s, the solid behaves as a viscous medium, as can be found by the comparison with the relaxation time of a viscoelastic body, given by the ratio of viscosity and rigidity of the solid,

$$\frac{\eta_s}{\mu} \sim 6\times 10^4\left(\frac{\eta_s}{10^{16}(\text{Pa s})}\right)\text{s},$$

from which we see that, for the time scale of interest, we may well assume viscous deformation. Also in the above formulation, we have assumed a linear relationship between pressure and deformation, i.e. Newtonian creep, rather than, say, power-law creep. This assumption is verified for the case of the inner core in Section 8.

The explicit form of the two constitutive relations, permeability and effective viscosity, as functions of porosity, are to be discussed in detail in Section 3.

We will assume 1-D Cartesian coordinates. From eqs (1) and (2) we can define the total volume flux, U, which is independent of z,

$$\phi v + (1-\phi)V \equiv U. \tag{6}$$

Eqs (4) and (5) can be rewritten in terms of ΔP and $\Delta\rho$, where $\Delta\rho \equiv \rho_s - \rho_f$, as

$$\frac{\partial}{\partial z}\{P_f + (1-\phi)\Delta P\} = -\{\rho_f + (1-\phi)\Delta\rho\}\mathbf{g}. \tag{7}$$

We can define solidity $\psi \equiv 1-\phi$, which we occasionally use to simplify the equations, and then the set of governing equations becomes

$$\frac{\partial \psi}{\partial t}+\frac{\partial}{\partial z}(\psi V)=0, \tag{8}$$

$$\frac{\eta_f}{K_\phi}(V-U)=-\left\{\frac{\partial}{\partial z}(\psi \Delta P)+\psi \Delta \rho g\right\}, \tag{9}$$

$$\Delta P=-\eta_\phi^* \frac{\partial V}{\partial z}. \tag{10}$$

Eq. (9) shows the balance of forces; the left-hand side is the viscous resistance of flow through the matrix, the first term on the right-hand side is the resistance to compaction and the second term denotes buoyancy.

The boundary conditions can be written with surface porosity ϕ_0, and the sedimentation rate $V_0(>0)$ as follows:

$$V=v=0 \qquad \text{at } z=0, \tag{11}$$

$$\Delta P=0 \qquad \text{at } z=h, \tag{12}$$

$$\phi=\phi_0 \qquad \text{at } z=h, \tag{13}$$

$$V(h)+V_0=\dot{h} \qquad \text{at } z=h. \tag{14}$$

Here $\dot{h}$ is the growth rate of the column of solid–fluid composite, which becomes smaller than the case when no compaction is occurring (i.e. $\dot{h}=V_0$), because of the subsidence of the matrix [i.e. $V(h)$]. The initial condition is $h=0$ at $t=0$. This situation is also illustrated in Fig. 1. Since we are only specifying the amount of solid flux being added to the top of the solid–fluid composite, and not *how* it is being added, this model represents both cases where the increase in height occurs by sedimentation and those where it occurs through dendritic growth.

Surface porosity is the largest porosity where the solid matrix can link together and form a mush. For porosity values larger than this, a slurry state is realized, which has no rigidity and does not propagate shear waves, and so we can assume that this corresponds to the inner-core boundary. The value of surface porosity is identical to the melt fraction at the rheological front of the solidifying magma (Solomatov & Stevenson 1993), which has a value of the rheological critical melt percentage (Arzi 1978) determined from the microscopic geometry of the sediment. For example, the surface porosity is ~ 0.7 for deep-sea sediments (Haq *et al.* 1990) whose solids form a spiny geometry, but it is $\sim 0.2 \pm 0.1$ (Arzi 1978) or ~ 0.29 (Toramaru & Fujii 1986) for magmatic systems. In most of the calculations in this paper, we take $\phi_0=0.5$ for analytical simplicity. The difference in surface porosity is not influential, as will be verified in Section 5.3. Our interest lies in solving a set of these equations, (8), (9) and (10), for different sedimentation rates $V_0(>0)$.

3 CONSTITUTIVE RELATIONS

There are two important constitutive relations in the above equations. They are the dependence of the *permeability*, K_ϕ, and the *effective viscosity*, η_ϕ^*, on porosity ϕ. The choice of constitutive relations is essential for quantitative arguments, but there is an uncertainty in its exact form. As noted in the introduction, we consider the state of a 'sponge' or 'mush' domain. It may be that the connectivity of the melt phase becomes small as the porosity decreases in the deeper parts of the inner core, and the melt phase becomes isolated to form a state of 'swiss cheese'. Such connectivity of the melt phase is not only a function of porosity but also of the interfacial energy, which is related to the light-element species. We have little knowledge of the details of such a microscopic texture at present, so we have not attempted to consider the state where complete isolation of fluid occurs, to avoid complexity. Nevertheless, we have used a strongly porosity-dependent formula for permeability, which we believe simulates its textural dependence.

3.1 Permeability

It should be noted that the porosity profiles obtained in the literature vary because the function which determines the efficiency of compaction differs. The constitutive relations usually used for sedimentary basins tend to make compaction difficult from two aspects: a strong porosity dependence of the permeability formula used, such as $K_\phi \propto \phi^8$, and a very small permeability at the surface, which is caused by a minute grain size of ~ 0.1 μm, as in the case for clay (Audet & Fowler 1992; Wangen 1992). On the other hand, those usually used for magma have a comparatively weak dependence on porosity and larger grains size of ~ 1 mm, making compaction easy to occur (McKenzie 1984).

Although the strict permeability of partial melt cannot be given unless the microscopic melt morphology is known, we adopt the commonly accepted Blake–Kozeny–Carman equation,

$$K_\phi=\frac{a^2\phi^3}{K(1-\phi)^2}, \tag{15}$$

which is known to represent the experimental data of permeability of magma quite well (McKenzie 1984). Here a is the grain size and K is the empirical constant of $10 \sim 1000$ representing tortuosity (McKenzie 1984). In this paper, we shall use this expression and take $K=1000$.

3.2 Effective bulk viscosity

We have described the matrix deformation as follows, using the effective bulk viscosity η_ϕ^*,

$$\Delta P \equiv P_s-P_f=-\eta_\phi^* \nabla \cdot \mathbf{V}=-\eta_\phi^* \frac{\partial V}{\partial z}. \tag{16}$$

The effective bulk viscosity of the matrix has not been experimentally measured, but can be derived theoretically as a function of porosity and solid shear vicosity, considering the deformation of the matrix as

$$\eta_\phi^*=\frac{4(1-\phi)}{3\phi}\eta_s \tag{17}$$

(see Appendix A for derivation). If we assume that at the surface porosity, the solid–fluid composite is in the state of 'Hertz contact', where an increase in porosity no longer allows the solid matrix to link together, the effective viscosity would drop to zero when the porosity becomes larger than the surface porosity. As a result, compaction no longer occurs for porosity larger than the surface porosity.

4 NON-DIMENSIONALIZATION OF BASIC EQUATIONS

We shall non-dimensionalize the governing equations by the following scales. The subscript 0 denotes the value at the surface. We will non-dimensionalize the velocity by the solid velocity when the fluid flows by its buoyancy alone, which we shall call the Darcy velocity,

$$V_D = \frac{K_{\phi_0}}{\eta_f}\psi_0 \Delta\rho g. \tag{18}$$

We take the length scale as the length scale determined by the balance of viscous resistance and compaction, the compaction length

$$L_C = \left(K_{\phi_0}\psi_0 \frac{\eta^*_{\phi_0}}{\eta_f}\right)^{1/2}. \tag{19}$$

Note that L_C is independent of gravity g and density difference $\Delta\rho$. For the time scale we use the time taken for the Darcy flow to flow the distance of the compaction length, the compaction time,

$$T_C = \frac{L_C}{V_D} = \frac{1}{\Delta\rho g}\left(\frac{\eta^*_{\phi_0}\eta_f}{K_{\phi_0}\psi_0}\right)^{1/2}. \tag{20}$$

We denote non-dimensional variables by circumflexes,

$$\hat{V} = V/V_D, \tag{21}$$

$$\hat{z} = z/L_C, \tag{22}$$

$$\hat{t} = t/T_C. \tag{23}$$

Then the governing equations (8), (9) and (10) become

$$\frac{\partial\psi}{\partial\hat{t}} + \frac{\partial}{\partial\hat{z}}\psi\hat{V} = 0, \tag{24}$$

$$\hat{V} - \hat{U} = \frac{K_\psi}{K_{\psi_0}}\left\{-\frac{\psi}{\psi_0} - \frac{\partial}{\partial\hat{z}}\left(\frac{\psi}{\psi_0}\Delta\hat{P}\right)\right\}, \tag{25}$$

$$\Delta\hat{P} = -\frac{\eta^*_\psi}{\eta^*_{\psi_0}}\frac{\partial\hat{V}}{\partial\hat{z}}. \tag{26}$$

The boundary conditions are

$$\hat{V} = \hat{v} = 0 \qquad \text{at } \hat{z} = 0, \tag{27}$$

$$\frac{\partial\hat{V}}{\partial\hat{z}} = 0 \qquad \text{at } \hat{z} = \hat{h}, \tag{28}$$

$$\phi = \phi_0 \qquad \text{at } \hat{z} = \hat{h}, \tag{29}$$

$$\hat{V} + \hat{V}_0 = \dot{\hat{h}} \qquad \text{at } \hat{z} = \hat{h}, \tag{30}$$

with the initial condition $\hat{h} = 0$ at $\hat{t} = 0$. Using the boundary condition (27), eq. (6) becomes $U = 0$, thus eq. (25) becomes

$$\hat{V} = \frac{K_\psi}{K_{\psi_0}}\left\{-\frac{\psi}{\psi_0} + \frac{\partial}{\partial\hat{z}}\left(\frac{\psi}{\psi_0}\frac{\eta^*_\psi}{\eta^*_{\psi_0}}\frac{\partial\hat{V}}{\partial\hat{z}}\right)\right\}, \tag{31}$$

which shows the force balance in the velocity scale. The left-hand side represents the viscous resistance, the first term on the right-hand side is the negative buoyancy term, and the second term is the deformation term. There are three types of force balance:

(1) Darcy balance: the left-hand side balances the first term on the right-hand side;

(2) squeezing balance: the left-hand side balances the second term on the right-hand side;

(3) deformation balance: the two terms on the right-hand side balance.

As we shall see in the solutions, the difference in the sedimentation rate results in different force balance structures. However, in reality the squeezing balance (2) does not occur. Note also that it is not the exact value of the permeability and effective viscosity but its functional dependence on porosity which is important in the qualitative results. Of course, such values are needed in quantitative arguments when transforming the results to the dimensionalized form.

5 TIME-DEPENDENT NUMERICAL SOLUTIONS

We will now solve eqs (24) and (31) numerically and see how the porosity structure evolves as a constant flux of partial melt is added on the top of the system. We use a finite-difference method for spatial discretization. Porosity is solved explicitly from eq. (24) and the solid velocity is solved from eq. (31). A staggered space grid is used; the porosity and the differential pressure are evaluated at the centre of the finite-difference volume, while the advection terms are evaluated at both ends of the volume. There are two changeable parameters: the porosity ϕ_0 at the surface, and the sedimentation rate, V_0. The calculated porosity profile takes a distinctively different form depending on whether the sedimentation rate is larger than or smaller than the Darcy velocity, V_D. This was noticed earlier by Shirley (1986) through solving a similar set of equations numerically, except that he did not make a distinction between the solid and the fluid pressures. Our calculated result generally agrees with his result, and we have also calculated the force balance and differential pressure structures so as to clarify the mechanics taking place.

5.1 Case for $V_0 > V_D$

First, let us consider the case for sedimentation rate larger than the Darcy velocity. The calculated result of the evolution of the porosity profile is given in Fig. 2(a). It can be seen that the porosity profile is time-dependent, characterized by two regions: an equi-porosity zone at the surface, and a gradually decreasing porosity towards the bottom. The equi-porosity region is in a state of uniform fluidization, as described by McKenzie (1984). Compaction does not occur and the liquid flows according to Darcy's law, driven only by buoyancy. From Fig. 2(c) it can be seen that at the surface, liquid percolates at the Darcy velocity and the solid matrix subsides uniformly at the same rate. We can see from the small value of the differential pressure gradient shown in Fig. 2(b) and from force balance (Fig. 2d) that Darcy balance predominates throughout the whole region. Hence, in this case, the decrease in porosity is driven by permeable flow and not by a differential pressure gradient. We will thus define the compaction occurring under Darcy balance as *percolative compaction*. Greater sedimentation rates result in the increase of the length of the equi-porosity region. A theoretical analysis is conducted in Section 6.2.

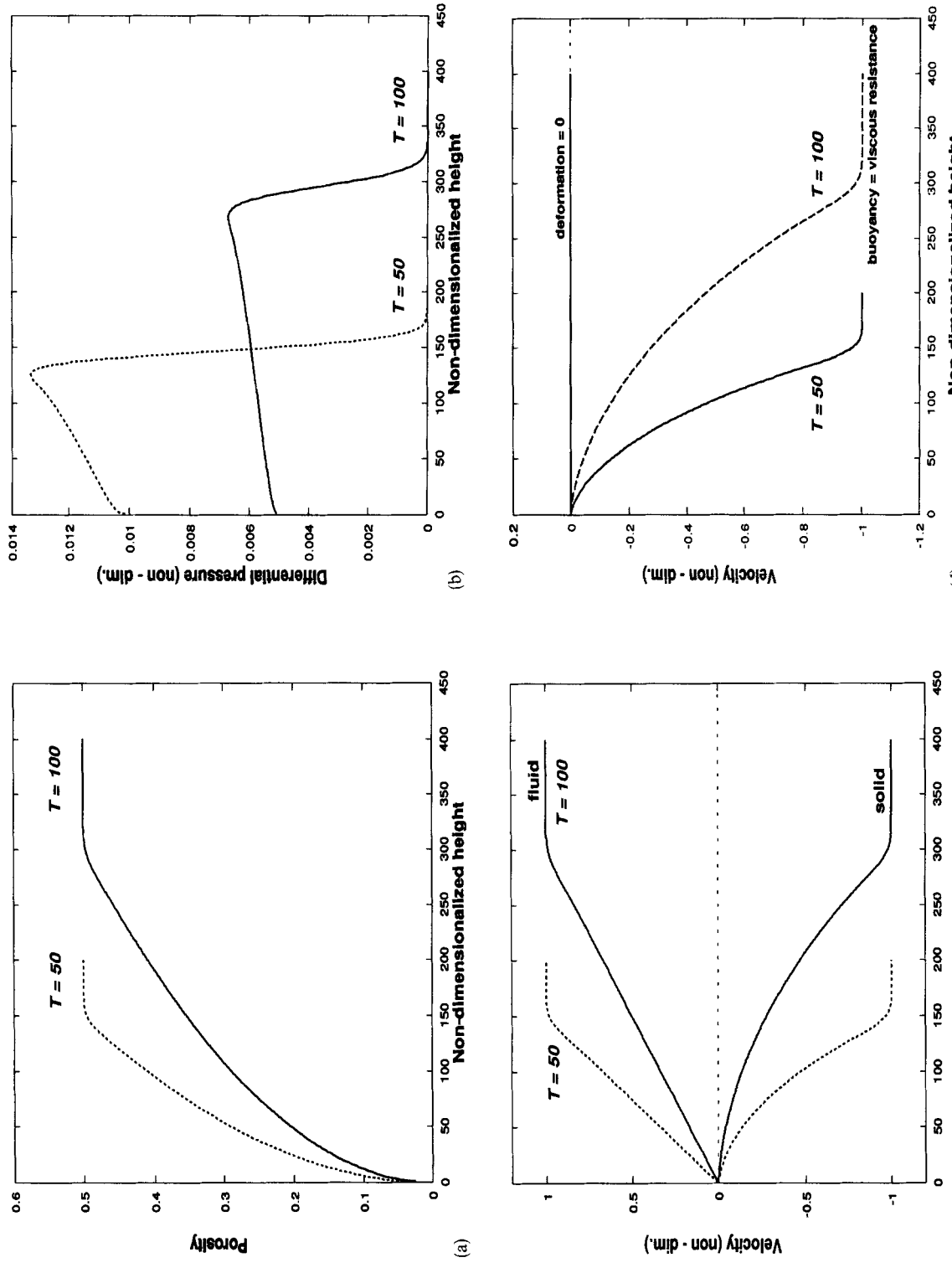

Figure 2. (a) Porosity structure for $\tilde{V}_0 = 5$, $\phi_0 = 0.5$, after 50 and 100 non-dimensionalized time (compaction time). Note that the structure is not stationary, and that there is an uncompacted region at the top which lengthens with time, with a gradually decreasing porosity towards the bottom. (b) Non-dimensionalized differential pressure structure for the condition corresponding to Fig. 2(a). The magnitude of the differential pressure is very small compared to the case where compaction is proceeding by deformation of the solid matrix (see Fig. 3b). (c) Solid and fluid velocity structure evolution for the condition corresponding to Fig. 2(a). Percolation occurs at Darcy velocity at the surface layer. (d) Force balance in velocity scale between the three terms of eq. (31) for $\tilde{V}_0 = 5$, $\phi_0 = 0.5$, after 50 and 100 non-dimensionalized time. We see that Darcy balance is established, i.e. the buoyancy term and the viscous resistance term are balanced.

5.2 Case for $V_0 < V_D$

A typical example of the porosity evolution for $V_0 < V_D$ is shown in Fig. 3(a). The profile here is characterized by three regions. The upper region, which we call the mushy layer, is where compaction is occurring. Its thickness does not change with time, therefore the porosity profile is stationary when seen from the coordinate which moves with the top boundary. We shall refer to this state as being quasi-stationary and call the thickness the *mushy-layer thickness*. We shall show later (eq. 76) that its magnitude is determined by the reduced compaction length L_R (Ribe 1985),

$$L_R = L_C \sqrt{\frac{V_0}{V_D}} = \sqrt{\frac{\eta^* V_0}{\Delta\rho g}}, \tag{32}$$

which is the compaction length for the system that has a boundary condition of $V = V_0$ with $V_0 < V_D$. However, the situation in Ribe (1985), who modelled the compaction of partial melting caused by upwelling mantle flow, is quite different from ours, in that the fluid velocity, instead of the solid velocity, is given as the boundary condition. The differential pressure profile is given in Fig. 3(b), and it shows that compaction is progressing within the mushy layer thickness. The force balance at this region is such that the negative buoyancy term roughly balances the deformation term forming the deformation balance, and decrease in porosity occurs, driven by the viscous deformation of the matrix (Fig. 3d). We will thus define the compaction occurring under deformation balance as *deformative compaction*. A theoretical analysis for this region is conducted in Section 6.3.

The middle region is characterized by constant porosity that does not change with time. We shall call this porosity the *residual porosity*. The matrix can no longer deform, due to the increase in effective viscosity and inefficient permeable flow, which is caused by the drastic decrease in permeability with depth. This state also corresponds to the state of uniform fluidization described by McKenzie (1984) and corresponds to the uniform fluidization porosity of Ribe (1985); this was termed 'abyssal' porosity in the study of sedimentary basins (Fowler 1990). In this region there is a permeable flow of liquid, but the solid matrix is hardly mobile (Fig. 3c). Here, the viscous resistance term balances the negative buoyancy term, forming a Darcy balance, and compaction ceases (Fig. 3e).

There is a region at the bottom where porosity gradually decreases again, which is driven by permeable flow and is in Darcy balance. This is thus in a state of percolative compaction and is the same phenomenon seen for the case for $V_0 > V_D$.

5.3 Effect of parameters

The effect of variation in sedimentation rate can be seen in Fig. 4(a) for a sedimentation rate near the Darcy velocity, and in Fig. 4(b) for a sedimentation rate smaller than the Darcy velocity. A larger sedimentation rate produces a greater mushy-layer thickness and residual porosity, due to lesser efficiency in expelling liquid, and these figures apply to the dimensionalized scale as well.

To see the effect of surface porosity, the effect of non-dimensionalizing scales must be taken into account, since the non-dimensionalizing scales are functions of surface porosity. Fig. 4(c) shows the surface-porosity dependence on the porosity structure when the solid flux $(1-\phi_0)V_0$ added to the top of the composite column is the same in the dimensionalized scale (see figure caption for details). As can be seen from the calculated results, the effect of surface porosity is not as marked as that of the sedimentation rate. Therefore we can conclude that the surface porosity values are not influential on the porosity structures formed when the sedimentation solid flux is constant.

The above results of parameter dependences are verified from the theoretical analysis given in Section 6.3.3. To summarize, there are three basic types of porosity profiles, according to the following sedimentation rates.

(1) $V_0 \gg V_D$. Non-stationary porosity profile characterized by two regions: (a) an upper region, with equi-porosity and Darcy balance; and (b) a lower region with porosity gradually decreasing downwards and percolative compaction occurring under Darcy balance.

(2) $V_0 \sim V_D$. Transitional type between a quasi-stationary and a non-stationary porosity profile.

(3) $V_0 \ll V_D$. Quasi-stationary porosity profile characterized by three regions: (a) an upper region with mushy layer, quasi-stationary, deformative compaction occurring under deformation balance; (b) a middle region with equi-porosity (residual porosity), no compaction and in Darcy balance; and (c) a lower region with porosity gradually decreasing downwards and, percolative compaction occurring under Darcy balance.

Here V_D is the Darcy velocity, as defined in eq. (18). This result shows that when the sedimentation rate changes from fast ($> V_D$) to slow ($< V_D$), the porosity profile shows a remarkable change.

6 THEORETICAL ANALYSIS

In order to understand the results of the numerical solutions, and to verify those results, it is of help to conduct a theoretical analysis. In this section we will perform a theoretical analysis in order to give physical and mathematical explanations for the numerical solutions obtained in the preceding section.

6.1 Linear analysis

First, let us investigate the dispersion relation of the basic equations. We take linear perturbation as

$$\psi = \psi_1 + \psi', \tag{33}$$

$$\hat{V} = -\left(\frac{1-\psi_1}{1-\psi_0}\right)^3 \frac{\psi_0}{\psi_1} + \hat{V}', \tag{34}$$

where ψ_1 is the solidity at the region of Darcy balance. Substituting the above expressions into eqs (24) and (31), we have

$$\frac{\partial \psi'}{\partial \hat{t}} = \left(\frac{1-\psi_1}{1-\psi_0}\right)^3 \frac{\psi_0}{\psi_1} \frac{\partial \psi'}{\partial \hat{z}} - \psi_1 \frac{\partial \hat{V}'}{\partial \hat{z}}, \tag{35}$$

$$\hat{V}' = \left(\frac{1-\psi_1}{1-\psi_0}\right)^3 \frac{\psi_0}{\psi_1} \frac{1+2\psi_1}{\psi_1(1-\psi_1)} \psi' + \left(\frac{1-\psi_1}{1-\psi_0}\right)^2 \frac{\partial^2 V'}{\partial \hat{z}^2}. \tag{36}$$

By eliminating ψ' from eqs (35) and (36), and assuming the following form for the perturbation term

$$\hat{V}' \propto \exp[i(w\hat{t} - k\hat{z})], \tag{37}$$

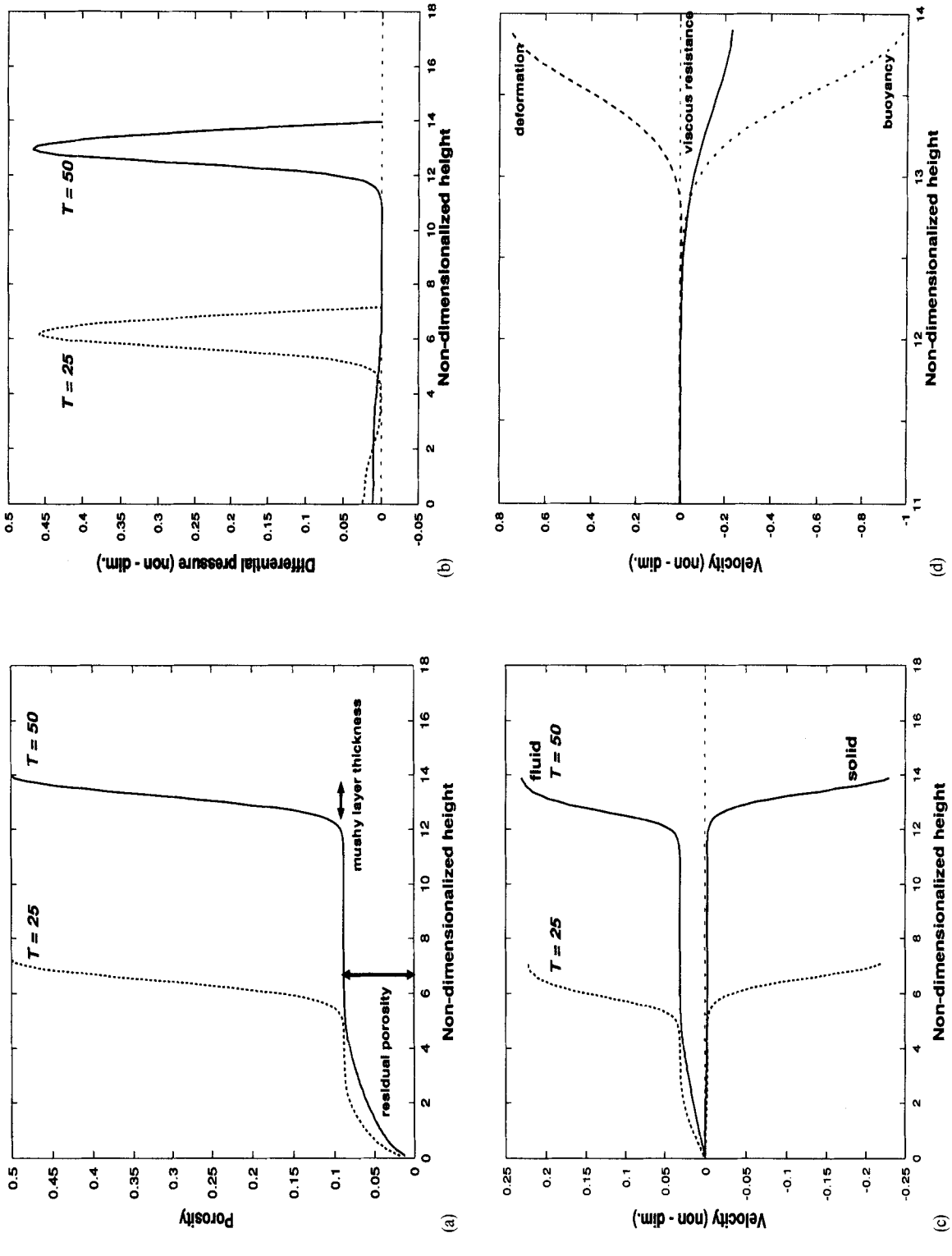

Figure 3. (a) Porosity evolution for $\hat{V}_0 = 0.5$, $\phi_0 = 0.5$ after 25 and 50 non-dimensionalized time. The profile can be considered as being quasi-stationary, characterized by mushy layer thickness and residual porosity. (b) Non-dimensionalized differential pressure structure between solid and liquid, $\Delta\hat{P} = -(\eta^*/\eta_{\psi_0^*})(\partial\hat{V}/\partial\hat{z})$, for the condition corresponding to Fig. 3(a). Compaction proceeds where the pressure difference is large. (c) Solid and fluid velocity distribution structure evolution for the condition corresponding to Fig. 3(a). Note that the fluid is flowing upwards, even at the region of residual porosity, while the solid hardly deforms. (d) Force balance in velocity scale between the three terms of eq. (31) at the region near the mushy layer (non-dimensionalized height of 11 to 14) for the condition corresponding to Fig. 3(a) and after 50 non-dimensionalized time. The figure shows that, in the region of the mushy layer, the buoyancy term roughly balances the deformation term, forming a deformation balance, and compaction proceeds. (e) Magnification of Fig. 3(d). At the region of residual porosity, the buoyancy term balances the viscous resistance term, forming Darcy balance, and compaction ceases.

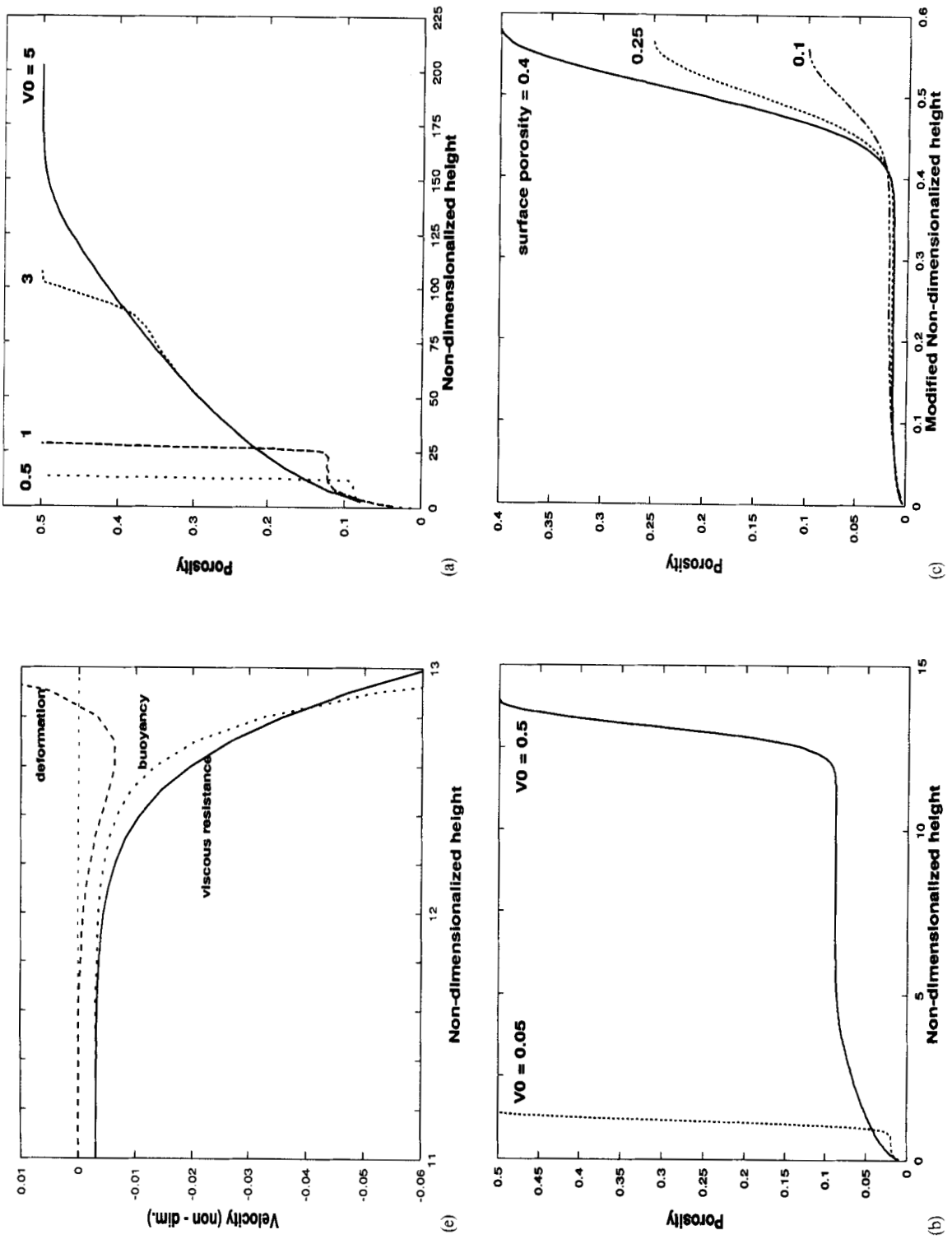

Figure 4. (a) Sedimentation rate dependence of porosity structures for $\hat{V}_0 = 0.5$ and $\hat{V}_0 = 1$, $\hat{V}_0 = 3$, $\hat{V}_0 = 5$ after 50 non-dimensionalized time. This shows the transition from the quasi-stationary solution to the non-stationary solution. (b) Sedimentation rate dependence of porosity structures for $\hat{V}_0 = 0.05$, $\hat{V}_0 = 0.5$, after 50 non-dimensionalized time. Note the difference in compaction length and residual porosity. (c) Surface porosity dependence of the porosity structure when the solid flux added to the top of the composite column in the dimensionalized scale is the same for three cases. Since the solid flux, $(1-\phi_0)V_0 \propto \phi_0^3 \hat{V}_0$, the value of $\hat{V}_0$ was altered for different ϕ_0, such that the solid flux is the same. The solid flux given is $\phi_0^3 \hat{V}_0 = 0.003$. The modified non-dimensionalized height is defined by $\phi_0 \times$ (non-dimensionalized height), such that it is proportional to the dimensionalized scale. Similarly, since $T_C \propto (1-\phi_0)/\phi_0^2$, the calculated non-dimensionalized times differ by $\propto \phi_0^2/(1-\phi_0)$, such that they are identical in the dimensionalized scale. The times elapsed are 2, 15 and 48 non-dimensionalized time for the cases where the surface porosities are 0.1, 0.25 and 0.4, respectively. As can be seen from the results, the magnitude of surface porosity does not significantly affect the magnitude of the mushy layer thickness, nor that of the residual porosity.

we get the dispersion relation

$$\frac{w}{k}=\frac{1-\phi_0}{\phi_0^3}\phi_1^2\frac{3-\left(\frac{\phi_1}{\phi_0}\right)^2\frac{\phi_1}{1-\phi_1}k^2}{1+\left(\frac{\phi_1}{\phi_0}\right)^2k^2}. \tag{38}$$

By expanding by k we get

$$\frac{w}{k}=\frac{1-\phi_0}{\phi_0}\phi_1^2\left\{3-\left(\frac{\phi_1}{\phi_0}\right)^2\frac{3-2\phi_1}{1-\phi_1}k^2+\cdots\right\}. \tag{39}$$

From the fact the dispersion effect begin with k^2, we can expect that the solution behaves analogously to the KdV equation, with some nonlinearity. By a reductive perturbation method, we can actually derive the KdV equation, as has been done by Whitehead & Helfrich (1986); the derivation is shown in Appendix B. In Section 6.3, we shall see that the solution can indeed be interpreted qualitatively in terms of the solitary wave.

6.2 Analysis of the percolative compaction region

A percolative compaction region was seen in both cases, $V_0 > V_D$ and $V_0 < V_D$. In both cases, percolative compaction occurred at the base of the column. Let us now make an attempt to provide an analytical solution of these regions.

6.2.1 Analytical solution

In the non-compacting region, since it is in Darcy balance, we can simplify the equations of mass and momentum conservation, by neglecting the deformation term, as

$$\frac{\partial\psi}{\partial\hat{t}}=-\frac{\partial}{\partial\hat{z}}(\psi\hat{V}), \tag{40}$$

$$\hat{V}=-\left(\frac{1-\psi}{1-\psi_0}\right)^3\frac{\psi_0}{\psi}. \tag{41}$$

Substituting eq. (41) into eq. (40), we get

$$\frac{\partial\psi}{\partial\hat{t}}=-3\frac{\psi_0}{1-\psi_0}\left(\frac{1-\psi}{1-\psi_0}\right)^2\frac{\partial\psi}{\partial\hat{z}}. \tag{42}$$

The results of the numerical calculation suggest the existence of a self-similar solution in the percolative compaction region. We therefore assume that the solution is only dependent on $\zeta=\hat{z}/\hat{t}$, to obtain

$$\frac{\partial}{\partial\hat{t}}=-\frac{\zeta}{\hat{t}}\frac{d}{d\zeta}, \tag{43}$$

$$\frac{\partial}{\partial\hat{z}}=\frac{1}{\hat{t}}\frac{d}{d\zeta}, \tag{44}$$

then the governing equation becomes

$$\zeta\frac{d\phi}{d\zeta}=3\frac{1-\phi_0}{\phi_0}\left(\frac{\phi}{\phi_0}\right)^2\frac{d\phi}{d\zeta}. \tag{45}$$

Through division of both sides of eq. (45) by $d\phi/d\zeta$, we get

$$\zeta=3\frac{1-\phi_0}{\phi_0}\left(\frac{\phi}{\phi_0}\right)^2. \tag{46}$$

Thus, besides the trivial solution of $\phi=\phi_0$, $\hat{V}=-1$ and $\Delta\hat{P}=0$, we can obtain the expressions for the time and space distribution of porosity, solid velocity and the differential pressure,

$$\phi=1-\psi=\phi_0\sqrt{\frac{\phi_0}{3(1-\phi_0)}\frac{\hat{z}}{\hat{t}}}, \tag{47}$$

$$\begin{aligned}\hat{V}&=-\left(\frac{\phi}{\phi_0}\right)^3\frac{1-\phi_0}{1-\phi}\\&=-\left\{\frac{\phi_0}{3(1-\phi_0)}\frac{\hat{z}}{\hat{t}}\right\}^{3/2}\frac{1-\phi_0}{1-\phi_0\sqrt{\frac{\phi_0}{3(1-\phi_0)}\frac{\hat{z}}{\hat{t}}}},\end{aligned} \tag{48}$$

$$\begin{aligned}\Delta\hat{P}&=-\frac{1-\phi}{1-\phi_0}\frac{\phi_0}{\phi}\frac{\partial\hat{V}}{\partial\hat{z}}\\&=\left\{3\frac{\phi}{\phi_0}+\left(\frac{\phi}{\phi_0}\right)^2\frac{\phi_0}{1-\phi}\right\}\frac{\partial}{\partial\hat{z}}\left(\frac{\phi}{\phi_0}\right)\\&=\frac{1}{2}\left(3\sqrt{\frac{\phi_0}{3(1-\phi_0)}\frac{\hat{z}}{\hat{t}}}+\frac{\phi_0}{3(1-\phi_0)}\frac{\hat{z}}{\hat{t}}\frac{\phi_0}{1-\phi_0\sqrt{\frac{\phi_0}{3(1-\phi_0)}\frac{\hat{z}}{\hat{t}}}}\right)\\&\quad\times\sqrt{\frac{\phi_0}{3(1-\phi_0)}\frac{1}{\hat{z}\hat{t}}}.\end{aligned} \tag{49}$$

6.2.2 Comparison of the numerical solution and theoretical analysis

Let us compare the results of the numerical solution obtained in Section 5 and the analytical solutions obtained above for the case of Darcy balance. First, let us consider the case for $V_0 > V_D$. The numerical solution obtained for $V_0 > V_D$ can be considered as being the combination of two solutions, eq. (47) and $\phi=\phi_0$. The reasons are as follows. When the surface porosity is $\phi_0=0.5$, the position of the solid–fluid composite above which the porosity is equal to the surface porosity ascends as $\hat{z}=3\hat{t}$, as can be seen from eq. (47) for $\phi=\phi_0=0.5$. Therefore for sedimentation rates that are larger than $\hat{V}_0=3-\hat{V}(h)=4$, an equi-porosity region develops at the surface that has the solution of surface porosity $\phi=\phi_0$ and Darcy velocity $\hat{V}=-1$. A comparison of the numerical and the theoretical solution is shown in Fig. 5(a) and the solutions are in good accordance with one another.

In the case for $V_0 < V_D$, we notice that the region below the mushy layer is changing in a similar way as the case for $V_0 > V_D$, as can be seen from Fig. 3(a). This can be explained theoretically as before, in terms of Darcy balance, as shown in Fig. 5(c).

6.3 Analysis of the deformative compaction region

Let us now proceed to the deformative compaction region, where deformation balance is established.

6.3.1 Formulation of a stationary solution

From the numerical calculations, we have seen that when $V_0 < V_D$, the region of the mushy layer is quasi-stationary and deformative compaction is occurring near the surface. Thus we require a stationary solution for mechanical sedimentary compaction. Let us look at the compacting system under deformation balance at a coordinate moving at the growth

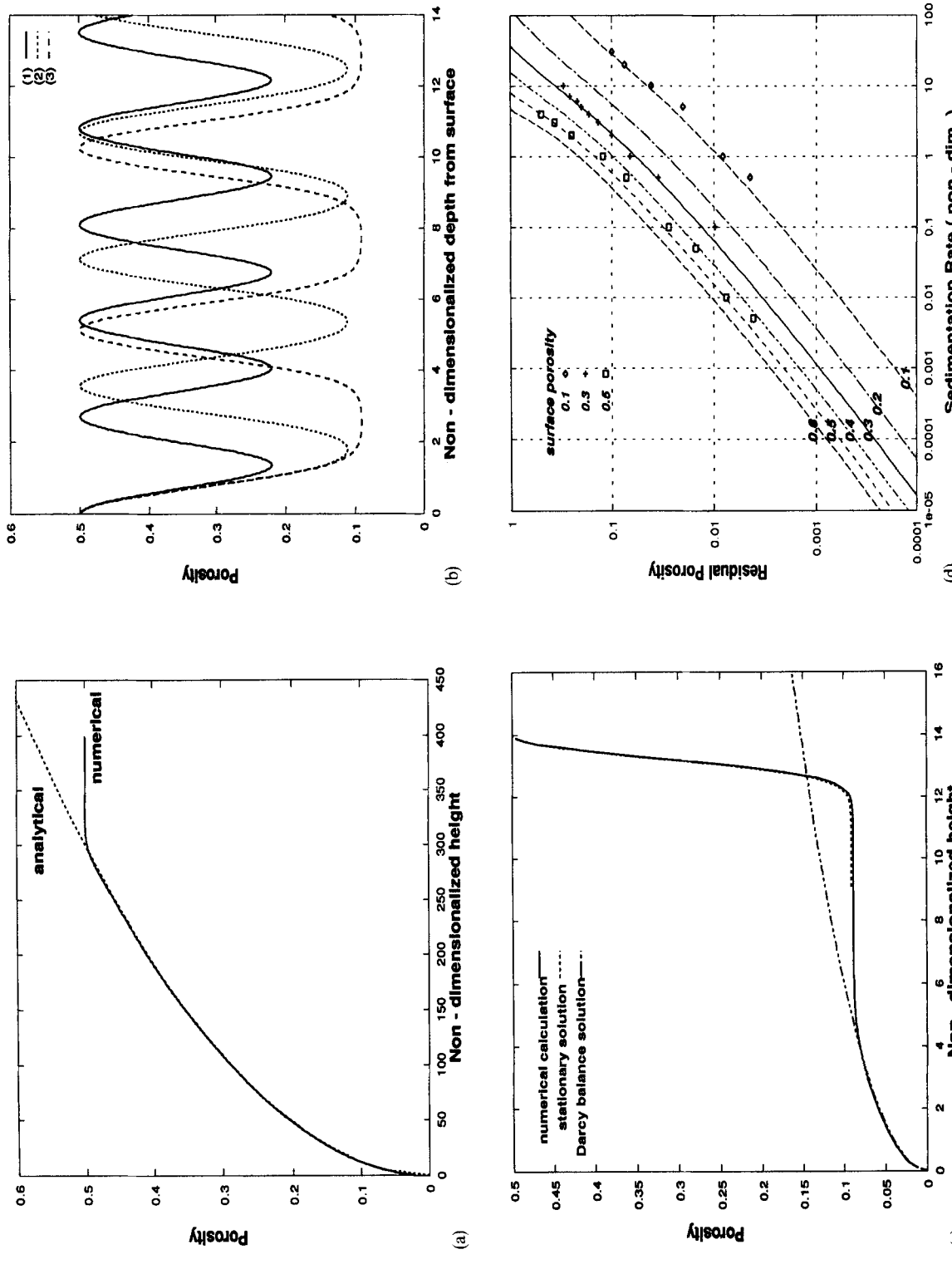

Figure 5. (a) Comparison of the analytical solution (eq. 47) and the numerical solution for $V_0 > V_D$, which forms Darcy balance. (b) A stationary cnoidal wave-like solution obtained by solving eq. (57). The fixed parameters are $\phi_0 = 0.5$ and $\hat{V}_0 = 0.5$. The porosity profiles are (1) $\hat{h} = 0.2$, (2) $\hat{h} = 0.27$, (3) $\hat{h} = 0.2715979$. (c) Comparison of the numerical solution with the stationary solution by solving eq. (57) and the theoretical solution eq. (47) for Darcy balance for the case of a sedimentation rate of $V_0 = 0.5$ and after 50 non-dimensionalized time. The numerical solution can be considered to be the combination of three solutions: the stationary solution, the constant porosity solution, and the Darcy balance solution. (d) Theoretical (eq. 65) and numerical non-dimensionalized sedimentation rate–residual porosity relations shown by curves (theoretical) and points (numerical). The curves are for surface porosities of $\phi_0 = 0.1$, 0.2, 0.3, 0.4, 0.5 and 0.6. Since the non-dimensionalizing velocity scale is a function of the surface porosity in the dimensionalized scale, the surface porosity dependence of residual porosity in the dimensionalized scale is actually small, as can be seen for the example in Fig. 4(c).

rate of the system $\dot{\hat{h}}$ (i.e. Lagrangian), and take the $\hat{z}$ axis positive upwards, with $\hat{z}=0$ at the surface. The formulation which follows is analogous to that performed in Scott & Stevenson (1984). As we shall see, the moving profile can be considered as the half-sided solitary wave.

We introduce ζ as

$$\zeta = \hat{z} - \dot{\hat{h}}\hat{t}, \tag{50}$$

and we assume that the solution depends only on ζ,

$$\frac{\partial}{\partial \hat{t}} = -\dot{\hat{h}}\frac{\partial}{\partial \zeta}, \tag{51}$$

$$\frac{\partial}{\partial \hat{z}} = \frac{\partial}{\partial \zeta}. \tag{52}$$

Then the non-dimensionalized basic equations (24) and (31) are transformed as

$$\dot{\hat{h}}\frac{\partial \psi}{\partial \zeta} = \frac{\partial}{\partial \zeta}(\psi \hat{V}), \tag{53}$$

$$\hat{V} = \frac{K_\psi}{K_{\psi_0}}\left\{-\frac{\psi}{\psi_0} + \frac{\partial}{\partial \zeta}\left(\frac{\psi}{\psi_0}\frac{\eta^*}{\eta_{\psi_0^*}}\frac{\partial \hat{V}'}{\partial \zeta}\right)\right\}. \tag{54}$$

From eq. (53) we get

$$\psi(\hat{V} - \dot{\hat{h}}) = -\psi_0 \hat{V}_0 = \text{const.} \tag{55}$$

Using eq. (55), the boundary condition given by eq. (28), $\partial \hat{V}/\partial \zeta = 0$, can be transformed into

$$\frac{\partial \phi}{\partial \zeta} = 0. \tag{56}$$

Using the expressions for permeability and effective viscosity, and by substituting eq. (54) into eq. (53) we get

$$\frac{\partial}{\partial \zeta}\left(\frac{1}{\phi}\frac{\partial \phi}{\partial \zeta}\right) = -\frac{1-\phi_0}{\phi_0}\left\{\frac{1}{\hat{V}_0}\frac{1-\phi}{1-\phi_0} + \left(\frac{\phi_0}{\phi}\right)^3\left(\frac{1-\phi}{1-\phi_0}\right)^2 \times \left(\frac{\dot{\hat{h}}}{\hat{V}_0} - \frac{1-\phi_0}{1-\phi}\right)\right\}. \tag{57}$$

The above equation shows the force balance. The balance between the first and second terms on the right-hand side shows the Darcy balance, the balance between the left-hand side and the second term on the right-hand side shows the squeezing balance, and the balance between the left-hand side and the first term on the right-hand side represents the deformation balance. We call the solution of this equation the stationary solution.

6.3.2 *Theoretical porosity profile and its parameter dependence*

Now let us focus our attention on finding the relation of the residual porosity and mushy layer thickness to sedimentation rate and surface porosity, and compare the results with the numerical solution. When sedimentation rate $\hat{V}_0$ and growth rate $\dot{\hat{h}}$ are given arbitrarily, eq. (57) can be solved numerically. The solution (Fig. 5b) is similar to a cnoidal wave solution of the KdV equation, unlike the solutions obtained earlier. This is because it lacks the boundary condition at the bottom.

By introducing $\Phi = -\ln \phi$, we can rewrite eq. (57) as

$$\frac{\partial^2 \Phi}{\partial \zeta^2} = \phi_0^2\left(1 - \frac{\dot{\hat{h}}}{(1-\phi_0)\hat{V}_0}\right)\exp 3\Phi + \phi_0^2\left(-1 + \frac{2\dot{\hat{h}}}{(1-\phi_0)\hat{V}_0}\right) \times \exp 2\Phi - \frac{\phi_0^2 \dot{\hat{h}}}{(1-\phi_0)\hat{V}_0}\exp \Phi + \frac{1}{\phi_0 \hat{V}_0} \times \exp(-\Phi) - \frac{1}{\phi_0 \hat{V}_0} \equiv f(\Phi). \tag{58}$$

Through the further introduction of $-\partial F(\Phi)/\partial \Phi = f(\Phi)$, the above equation can be transformed as

$$\frac{d}{d\zeta}\left[\frac{1}{2}\left(\frac{d\Phi}{d\zeta}\right)^2 + F(\Phi)\right] = 0. \tag{59}$$

Here,

$$F(\Phi) = \frac{\phi_0^2}{3}\left(1 - \frac{\dot{\hat{h}}}{(1-\phi_0)\hat{V}_0}\right)\exp 3\Phi + \frac{\phi_0^2}{2}\left(-1 + 2\frac{\dot{\hat{h}}}{(1-\phi_0)\hat{V}_0}\right) \times \exp 2\Phi - \frac{\phi_0^2 \dot{\hat{h}}}{(1-\phi_0)\hat{V}_0}\exp \Phi - \Phi\frac{1}{\phi_0 \hat{V}_0} - \frac{1}{\phi_0}\frac{1}{\hat{V}_0} \times \exp(-\Phi) + \text{const.} \tag{60}$$

The first term of eq. (59) is analogous to kinetic energy and the second term to potential energy. At $\zeta = -\infty$ we require $\partial \phi/\partial \zeta = \partial^2 \phi/\partial \zeta^2 = 0$, which makes $f(\Phi_{-\infty}) = 0$ and kinetic energy $\frac{1}{2}(d\Phi/d\zeta)^2 = 0$. The stress-free condition, eq. (56), gives the kinetic energy to be 0, i.e. $\frac{1}{2}(d\Phi/d\zeta)^2 = 0$ at the surface. Therefore, in order to solve the residual porosity, we have to solve the following equations simultaneously:

$$\frac{dF(\Phi_{-\infty})}{d\Phi} = f(\Phi_{-\infty}) = 0, \tag{61}$$

$$F(\Phi_0) = F(\Phi_{-\infty}), \tag{62}$$

which becomes

$$\phi_0^2\left(1 - \frac{\dot{\hat{h}}}{(1-\phi_0)\hat{V}_0}\right)\exp 3\Phi_r + \phi_0^2\left(-1 + \frac{2\dot{\hat{h}}}{(1-\phi_0)\hat{V}_0}\right)\exp 2\Phi_r - \frac{\phi_0^2 \dot{\hat{h}}}{(1-\phi_0)\hat{V}_0}\exp \Phi_r + \frac{1}{\phi_0 \hat{V}_0}\exp(-\Phi_r) - \frac{1}{\phi_0 \hat{V}_0} = 0, \tag{63}$$

$$\frac{\phi_0^2}{3}\left(1 - \frac{\dot{\hat{h}}}{(1-\phi_0)\hat{V}_0}\right)(\exp 3\Phi_0 - \exp 3\Phi_r) + \frac{\phi_0^2}{2}\left(-1 + 2\frac{\dot{\hat{h}}}{(1-\phi_0)\hat{V}_0}\right)(\exp 2\Phi_0 - \exp 3\Phi_r) - \frac{\phi_0^2 \dot{\hat{h}}}{(1-\phi_0)\hat{V}_0}(\exp \Phi_0 - \exp \Phi_r) - (\Phi_0 - \Phi_r)\frac{1}{\phi_0 \hat{V}_0} - \frac{1}{\phi_0}\frac{1}{\hat{V}_0}[\exp(-\Phi_0) - \exp(-\Phi_r)] = 0. \tag{64}$$

Here $\phi_r = \phi_{-\infty}$ denotes the residual porosity. By eliminating $\dot{\hat{h}}$, we derive the following equation:

$$0 = \frac{1}{\hat{V}_0}\left[\left\{\phi_r - \phi_0 - \ln\left(\frac{\phi_r}{\phi_0}\right)\right\} - \frac{1}{3}\frac{\phi_r^3}{1-\phi_r}\left\{\left(\frac{1-\phi_r}{\phi_r}\right)^3 - \left(\frac{1-\phi_0}{\phi_0}\right)^3\right\}\right]$$

$$+\frac{\phi_0^2}{3}\frac{1}{1-\phi_r}\left\{\left(\frac{1-\phi_r}{\phi_r}\right)^3-\left(\frac{1-\phi_0}{\phi_0}\right)^3\right\}$$

$$+\phi_0^2\left\{-\frac{1}{3}\left(\frac{1}{\phi_r^3}-\frac{1}{\phi_0^3}\right)+\frac{1}{2}\left(\frac{1}{\phi_r^2}-\frac{1}{\phi_0^2}\right)\right\}, \tag{65}$$

which shows the sedimentation rate and surface porosity dependence of the residual porosity.

When we approximate the above relationship, when $\phi_r \ll \phi_0 < 1$, we get the following expression:

$$0=\frac{1}{\hat{V}_0\phi_0}\ln\left(\frac{\phi_0}{\phi_r}\right)-\frac{1}{6}\left(\frac{\phi_0}{\phi_r}\right)^2, \tag{66}$$

which becomes

$$\hat{V}_0=6\frac{1}{\phi_0}\left(\frac{\phi_r}{\phi_0}\right)^2\ln\left(\frac{\phi_0}{\phi_r}\right). \tag{67}$$

We can assume that $\ln(\phi_0/\phi_r)$ does not vary very much for the parameter range of interest, and the simplified relation becomes

$$\phi_r \propto \sqrt{\hat{V}_0\phi_0^3}. \tag{68}$$

We can derive the growth rate of the system as follows. The solid velocity at the region of residual porosity is

$$\hat{V}_r=-\left(\frac{\phi_r}{\phi_0}\right)^3\frac{1-\phi_0}{1-\phi_r}\approx-\left(\frac{\phi_r}{\phi_0}\right)^3(1-\phi_0). \tag{69}$$

From eq. (55), we have

$$\dot{\hat{h}}=\hat{V}_r+\frac{1-\phi_0}{1-\phi_r}\hat{V}_0\approx\hat{V}_r+(1-\phi_0)\hat{V}_0. \tag{70}$$

Using the above two equations we get

$$\dot{\hat{h}}\approx(1-\phi_0)\hat{V}_0=6\frac{1-\phi_0}{\phi_0}\left(\frac{\phi_r}{\phi_0}\right)^2\ln\left(\frac{\phi_0}{\phi_r}\right). \tag{71}$$

It is also possible to obtain the mushy layer thickness as a function of these parameters. At the surface we have, from the boundary condition,

$$\phi=\phi_0, \tag{72}$$

$$\frac{\partial\phi}{\partial\zeta}=0, \tag{73}$$

the latter of which was derived in eq. (56). Thus we can approximate eq. (57) near the surface as

$$\frac{\partial^2\phi}{\partial\zeta^2}=(1-\phi_0)\left(\frac{1+\dot{\hat{h}}-\hat{V}_0}{\hat{V}_0}\right). \tag{74}$$

From eq. (74) we see that the mushy layer thickness is given by

$$\sqrt{\frac{\phi_0}{1-\phi_0}\frac{\hat{V}_0}{1+\dot{\hat{h}}-\hat{V}_0}}\approx\sqrt{\frac{\phi_0}{1-\phi_0}\frac{\hat{V}_0}{1+\phi_0\hat{V}_0}}\qquad(\phi_r\ll\phi_0<1)$$

$$\approx\sqrt{\frac{\phi_0}{1-\phi_0}\hat{V}_0}. \tag{75}$$

The approximation in eq. (75) is valid when compaction is efficient, i.e. when permeability is large or sedimentation rate is small.

6.3.3 *Comparison of numerical solutions and theoretical analysis*

Let us now compare the numerical and theoretical solutions in the deformative compaction region. Fig. 5(c) shows the comparison of numerical and stationary solutions for $V_0 < V_D$ and shows that they are in good agreement with each other. The solutions were obtained by using the stationary solution eq. (57) for the mushy layer, constant porosity solution for the residual porosity region, and the Darcy balance solution (eq. 47) for the deepest region.

Fig. 5(d) shows the relationship between the sedimentation rate, $\hat{V}_0$, and the residual porosity, ϕ_r, for cases with particular surface porosities ϕ_0. From this diagram we can see that the numerical and theoretical solutions (eq. 65) agree well with each other, allowing us to conclude safely that the numerical solution can be considered as being quasi-stationary when the sedimentation rate is less than the Darcy velocity. We can use Fig. 5(d) to estimate the value of the residual porosity under given sedimentation rate and surface porosity. When $\phi_r \ll \phi_0$, we can use eq. (68) as a simplified relation between the sedimentation rate and the residual porosity. By transforming eqs (75) and (68) to the dimensionalized relations we get,

$$\text{mushy layer thickness} \sim \sqrt{\frac{4\eta_s}{3\Delta\rho g}V_0}, \tag{76}$$

$$\text{residual porosity} \propto \sqrt{\frac{\phi_0^3\eta_f V_0}{K_{\phi_0}(1-\phi_0)\Delta\rho g}}. \tag{77}$$

From these relations we can see how parameters such as η_f, η_s and K_{ϕ_0} affect the typical values above. Note that eq. (76) is approximately the same as eq. (32).

It should be noted that the relation of the sedimentation rate to the mushy layer thickness is independent of the permeability and surface porosity, while it is linearly proportional to the square root of the solid viscosity. This parameter dependence occurs because deformation balance is occurring at this region and the ability of the solid matrix to deform controls the rate of compaction in this domain. In McKenzie (1987) the position of the base of the mushy layer was named the compaction front. He showed that, if the amount of subsidence caused by compaction is known from the field observations of dykes, one can estimate the solid viscosity and the sedimentation rate of the formed composite.

The magnitude of the residual porosity, on the other hand, is proportional to the square root of the ratio of the fluid viscosity to the surface permeability, and becomes larger with decreasing permeability. This dependence is because the magnitude of the Darcy velocity, i.e. the ability of the liquid to percolate, controls the porosity in this domain. It should be noted that when we use the Blake–Kozeny–Carman formula for permeability, as shown in eq. (15), the magnitude of the residual porosity becomes independent of the magnitude of surface porosity, under the condition that the precipitating solid flux $(1-\phi_0)V_0$ is constant, as was shown in Fig. 4(c).

It is interesting to see that each of the two characteristic scales shown above contain different and independent information about material properties, while they are both dependent on the sedimentation rate. Also, as has been shown in Section 5.3, surface porosity is not influential on the characteristic features of the porosity structure. Therefore, we shall not consider its effects further, but focus our attention on the structural dependences on sedimentation rate, viscosity and permeability, which can vary by several orders of magnitude for a variety of geophysical phenomena (see Table 2).

Finally, we can estimate the magnitude of the pressure difference, ΔP, between the solid and the fluid, which is driving

Table 2. List of parameters.

Variable	Meaning	inner core	magma chamber,ocean	sediment	Dimensions
a	grain size	$> 10^{-8}$	10^{-3}(a)	$> 10^{-8}$	m
g	gravitational acceleration	4.4(b)	9.8	9.8	ms^{-2}
K_ϕ	permeability	$> 10^{-20}$	10^{-10}	$10^{-20\sim-12}$	m^2
V_0	sedimentation rate	$\geq 10^{-12}$	10^{-8}(c), 10^{-5}(d)	$10^{-13\sim-10}$	ms^{-1}
V_D	Darcy velocity	$\geq 10^{-14}$	10^{-8}	$10^{-7\sim-5}$	ms^{-1}
L_C	compaction length	$\geq 10^{-1}$	10^2	$10^{0\sim4}$	m
L_R	reduced compaction length	> 1	$10^2, 10^3$	$10^{0\sim3}$	m
T_C	compaction time	$< 10^{13}$	10^{10}	$10^{11\sim15}$	s
z	length scale	1.22×10^6	$\sim 10^3, \sim 10^6$	$\sim 10^3$	m
η_s	shear viscosity of solid	$\geq 10^{16}$(e)	10^{15}(a)	$\sim 10^{21}$	Pas
η_f	shear viscosity of fluid	1.22×10^{-3}	1(a)	10^{-3}	Pas
ϕ_0	surface porosity	0.4	$\sim 0.2 \pm 0.1$(f)	~ 0.7	none
ρ_s	solid density	1.276×10^4(b)	3.3×10^3(a)	$\sim 2.5 \times 10^3$	kgm^{-3}
ρ_f	fluid density	1.216×10^4(b)	2.8×10^3(a)	$\sim 1.0 \times 10^3$	kgm^{-3}
$\Delta\rho$	$\rho_s - \rho_f$	6.0×10^2(b)	5×10^2(a)	$\sim 10^3$	kgm^{-3}

(a) McKenzie (1984)
(b) at present ICB (1220.0 km) : Dziewonski and Anderson (1981)
(c) for Muskox Intrusion : Irvine (1980)
(d) Tonks and Melosh (1990)
(e) Yoshida, Sumita and Kumazawa (1996) : $\eta_s = 8 \times 10^{21}$ was used for the numerical calculations of the inner core
(f) Arzi (1978)

the deformation. Since most of the compaction occurs at the length scale of the mushy layer, we can estimate it as

$$\Delta P = -\eta_\phi^* \nabla \cdot \mathbf{V} \sim \eta_s \frac{V_0}{\text{mushy layer thickness}} \sim \sqrt{\Delta\rho g \eta_s V_0}. \tag{78}$$

We shall use this estimate for the inner core in Section 8.

7 SEDIMENTARY COMPACTION IN A SELF-GRAVITATING SPHERE

If we are to apply the physics of sedimentary compaction to the Earth's inner-core growth process, we must consider three additional effects: spherical geometry, radial dependence of the gravity, and time dependence of the sedimentation rate. In this section we shall see how the results of the columnar case studied above are affected by these effects. This system is non-stationary, and it is in such cases that numerical solutions become particularly useful.

We can rewrite the basic equations in spherical coordinates:

$$\frac{\partial \psi}{\partial t} + \frac{1}{r^2}\frac{\partial}{\partial r}(r^2 \psi V) = 0, \tag{79}$$

$$V = -\frac{K_\phi}{\eta_f}\left\{\frac{\partial}{\partial r}(\psi \Delta P) + \psi \Delta\rho g\right\}, \tag{80}$$

$$\Delta P = -\eta_\phi^* \frac{1}{r^2}\frac{\partial}{\partial r}(r^2 V). \tag{81}$$

We shall non-dimensionalize the above equations with the same scales as before, and obtain

$$\frac{\partial \psi}{\partial \hat{t}} + \frac{1}{\hat{r}^2}\frac{\partial}{\partial \hat{r}}(\hat{r}^2 \psi \hat{V}) = 0, \tag{82}$$

$$\hat{V} = -\frac{K_\psi}{K_{\psi_0}}\left\{\frac{\psi}{\psi_0}\frac{g(\hat{r})}{g(\hat{R})} + \frac{\partial}{\partial \hat{r}}\left(\frac{\psi}{\psi_0}\Delta\hat{P}\right)\right\}, \tag{83}$$

$$\Delta\hat{P} = -\frac{\eta_\psi^*}{\eta_{\psi_0}^*}\frac{1}{\hat{r}^2}\frac{\partial}{\partial \hat{r}}(\hat{r}^2 \hat{V}). \tag{84}$$

Here $g(r) = 4\pi G\rho r/3$, and R is the reference radius taken for the gravity value used for non-dimensionalization, hence

$$\frac{g(\hat{r})}{g(\hat{R})} = \frac{\hat{r}}{\hat{R}}.$$

In the numerical calculations which follow, we shall study the case for $V_0 < V_D$ where compaction balance forms, to see the three separate effects. We shall add the three effects mentioned above one after another in the following discussions.

First we will investigate the effect of spherical geometry. We keep g and V_0 constant: $g = g(R)$ and $V_0 = 0.5V_D$. Let us compare sedimentary compaction in a sphere to that in a column. As can be seen from comparing Figs 3(a) and 6(a), whose sedimentation rates are the same, the mushy-layer thicknesses are identical in both cases when the sphere becomes large enough, while in the region of residual porosity, the spherical geometry forbids residual porosity to remain constant with depth. As a result, the porosity becomes smaller in a sphere than in a column. These results can be understood as follows. The effect of spherical geometry becomes negligible for the mushy layer because the radius of the sphere is much larger than the mushy layer thickness. On the other hand, the reason for a monotonically decreasing residual porosity

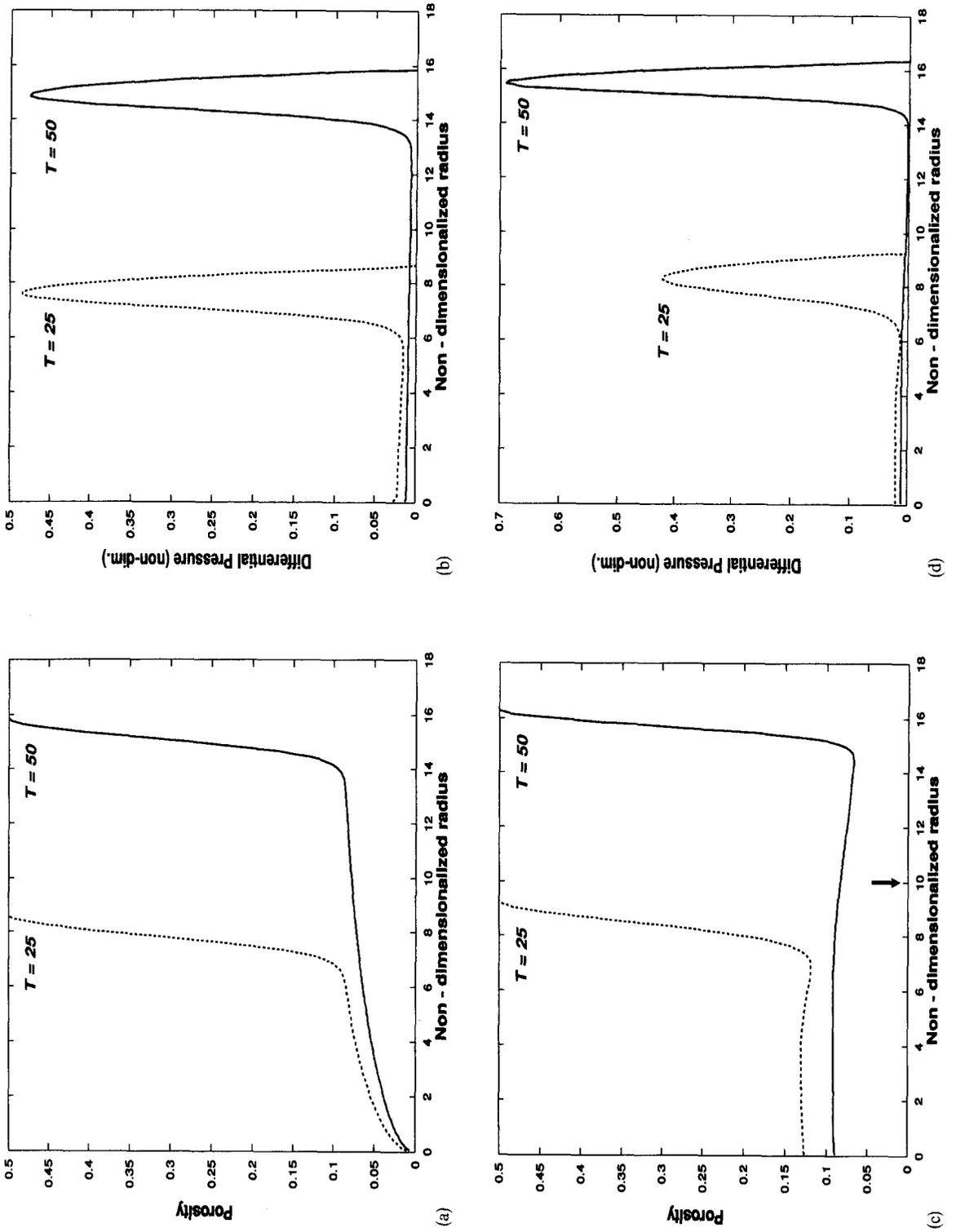

Figure 6. (a) Porosity evolution in a sphere with a constant sedimentation rate of $\hat{V}_0 = 0.5$, $\phi_0 = 0.5$, and without the effect of radially dependent gravity. The dotted curve is for $\hat{t} = 25$ and the solid curve for $\hat{t} = 50$. Note the radius-dependent residual porosity as compared to the case for a column (Fig. 3a). (b) Differential pressure evolution in a sphere after 25 and 50 non-dimensionalized time for the condition corresponding to Fig. 6(a). Note the non-zero differential pressure at the region of residual porosity and larger peak differential pressure, as compared to that of a column (Fig. 3b). (c) Porosity evolution in a sphere with a constant sedimentation rate of $\hat{V}_0 = 0.5$, $\phi_0 = 0.5$, and with the effect of radially dependent gravity after 25 and 50 non-dimensionalized time. The reference radius of the gravity value is $\hat{r} = 10$, as indicated by an arrow. Note the larger residual porosity than that with constant gravity (Fig. 6a) due to smaller gravity. (d) Differential pressure evolution in a sphere for the condition corresponding to Fig. 6(c). Note the increase in differential pressure with the increase of the inner core radius, due to increase in gravity. (e) Porosity evolution in a sphere with the effect of radially dependent gravity and a constant volumetric sedimentation rate of 200 non-dimensionalized volume per unit time. This corresponds to an initial sedimentation rate of $\hat{V}_0 = 78.2$, which decreases inversely proportionally to the square of the radius of the growing sphere. The profiles are those at 100 and 200 non-dimensionalized time. The reference radius of the gravity value is $\hat{r} = 10$, as indicated by the arrow. Note the unstable porosity structure at the region just below the mushy layer, and the appearance of a solitary wave packet, which formed due to the substantial decrease in sedimentation rate. (f) Differential pressure evolution in a sphere for the condition corresponding to Fig. 6(e). The profiles are those at 100 and 200 non-dimensionalized time. Note the decompaction occurring (the region with negative differential pressure) due to the upwelling of the fluid-rich solitary wave packet. The negative differential pressure, together with the positive one, forms a 'pressure dipole'. Note the increase in the magnitude of the pressure dipole and steepening of the solitary wave with time.

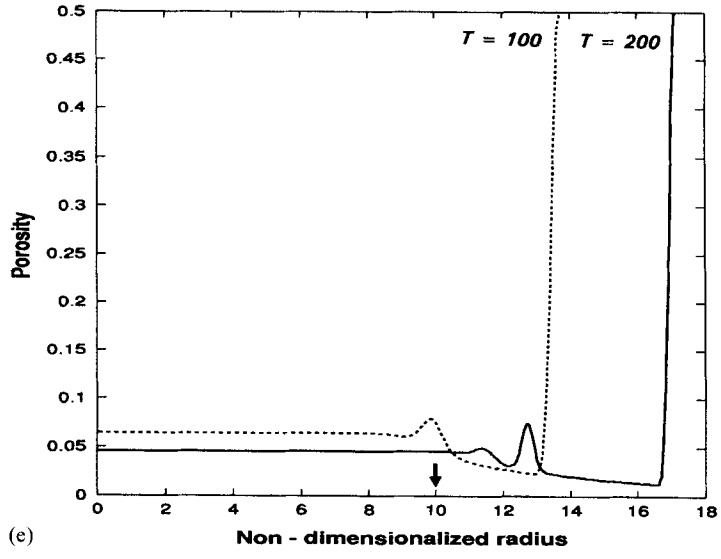

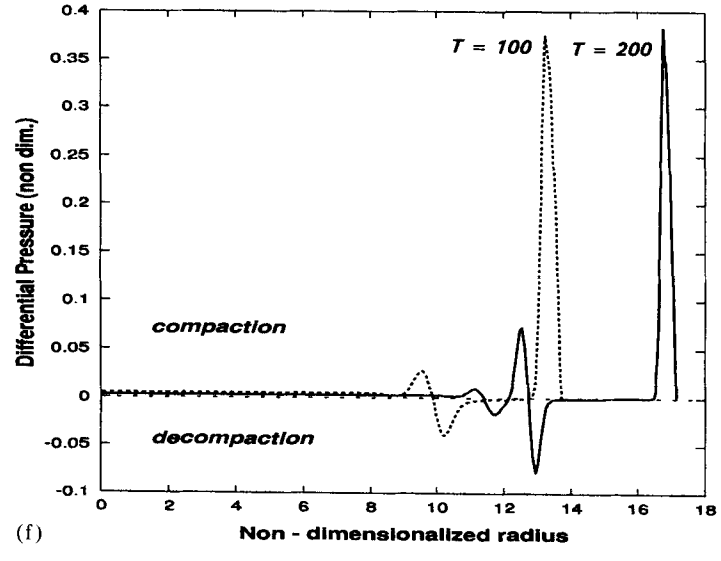

Figure 6. (e) Porosity evolution in a sphere with the effect of radially dependent gravity and a constant volumetric sedimentation rate of 200 non-dimensionalized volume per unit time. This corresponds to an initial sedimentation rate of $\hat{V}_0 = 78.2$, which decreases inversely proportionally to the square of the radius of the growing sphere. The profiles are those at 100 and 200 non-dimensionalized time. The reference radius of the gravity value is $\hat{r} = 10$, as indicated bu the arrow. Note the unstable structure at the region just below the mushy layer, and the appearance of a solitary wave packet, which formed due to the subbstantial decrease in sedimentation rate. (f) Differential pressure evolution in a sphere for the condition corresponding to Fig. 6(e). The profiles are those at 100 and 200 non-dimensionalized time. Note the decompaction occuring (the region with negative differential pressure) due to the upwelling of the fluid-rich solitary wave packet. The negative differential pressure, together with the positive one, forms a 'pressure dipole'. Note the increase in the magnitude of the pressure dipole and steepening of the solitary wave with time.

with depth is as follows. As can be seen from the equation of continuity, if the porosity and solid velocity remain approximately constant with depth, from eq. (82) we get

$$\frac{\partial \phi}{\partial \hat{t}} \propto -\frac{1}{\hat{r}} < 0$$

(note that $\hat{V}$ is negative), which means that the porosity decrease is enhanced in the deeper parts (where the radius is small), hence the porosity must inevitably decrease with depth. When we examine the differential pressure profile in Fig. 6(b), we find that the peak differential pressure is larger and that the differential pressure is non-zero at the region of residual porosity, compared to Fig. 3(b). These are consequences of the spherical geometry enhancing compaction.

Second, let us now add the effect of the radially dependent gravity to the results obtained above. As can be seen from Fig. 6(c), in the case of the gravity proportional to the radius, compaction is not efficient at the centre of the Earth where the gravity is zero, and creates a larger residual porosity than in the case of constant gravity (Fig. 6a). The differential pressure in the mushy layer also increases with sphere radius, as can be seen from Fig. 6(d). Another important result is that

the gravity proportional to the radius causes the residual porosity to remain constant with depth. Let us check that the depth-independent solution of the porosity structure actually exists. We assume that the region of the residual porosity is in Darcy balance

$$\hat{V} = -\frac{K_\psi}{K_{\psi_0}} \frac{\psi}{\psi_0} \frac{g(\hat{r})}{g(\hat{R})}. \tag{85}$$

From eq. (84)

$$\Delta \hat{P} = -\frac{\eta_\psi^*}{\eta_{\psi_0}^*} \frac{1}{\hat{r}^2} \frac{\partial}{\partial \hat{r}} (\hat{r}^2 \hat{V}) = \text{independent of } \hat{r}. \tag{86}$$

Therefore the Darcy balance solution (eq. 85) satisfies eq. (83), and this is true only if the gravity is proportional to the radius. By substituting eq. (85) into eq. (82) we obtain

$$\frac{\partial \psi_r}{\partial \hat{t}} = -\frac{1}{\hat{r}^2} \frac{\partial}{\partial \hat{r}} (\hat{r}^2 \psi_r \hat{V})$$

$$= \frac{3}{\hat{R}} \frac{K_{\psi_r}}{K_{\psi_0}} \frac{\psi_r^2}{\psi_0} \quad \propto (1 - \psi_r)^3, \tag{87}$$

from which we see that

$$\frac{\partial \phi_r}{\partial \hat{t}} \propto -\phi_r^3, \tag{88}$$

hence

$$\phi_r \propto \frac{1}{\sqrt{\hat{t}}} (\hat{t} \to \infty). \tag{89}$$

Therefore, the residual porosity decreases uniformly (i.e. independently of depth) and inversely proportionally to the square root of time.

Third, let us add the change of sedimentation rate with the sphere radius. For a constant volumetric sedimentation rate, which is more realistic for the inner core, the 1-D sedimentation rate, V_0, is inversely proportional to the square of the sphere radius, and the sedimentation rate decreases with radius. This produces an unstable porosity structure because residual porosity is larger at the deeper parts due to a greater sedimentation rate in the past. From Fig. 6(e) the effect of decreasing sedimentation rate is apparent as the decrease in residual porosity near the surface. A minimum porosity, or a trough porosity, exists at the bottom of the mushy layer, and this corresponds to the residual porosity of the recent sedimentation rate. Unstable porosity structure may result in the formation of solitary waves at the region of residual porosity, as can be seen from Fig. 6(e). Formation of solitary waves can be understood as follows. From the dispersion relation of eq. (39), we can see that the porosity profile changes more rapidly in the region of larger porosity. Therefore the porosity profile steepens if porosity increases with depth. The steepening eventually balances the dispersion effect proportional to k^2 to form a solitary wave. Formation of the solitary wave is manifested by decompaction, where porosity increases with time and a bulge of fluid packet forms (Fig. 6f). This differential pressure structure of a pair of positive and negative ones may be referred to as a 'pressure dipole', as described by Ida & Kumazawa (1986). The appearance of solitary waves in a sedimentary compacting system was noticed by McKenzie (1987) in the case of constant sedimentation on a partially molten column. We have now discovered that an unstable structure and solitary waves form also in a system of monotonically decreasing sedimentation rate. Such waves can form through the inner core growth process, and sedimentation of particles in magma chambers can affect their dynamics.

We have seen from the analysis of the Darcy balance in a self-gravitating sphere that the porosity inevitably decreases with time, even in the region of Darcy balance. This means not only that the residual porosity decreases with time, but also that the constant porosity layer near the surface, when $V_0 > V_D$ in the case of a column (Fig. 2a), no longer exists. Instead, even for the case of $V_0 > V_D$, the deformation term contributes to the force balance near the surface, which becomes more evident as the buoyancy term increases (proportionally to the radius) with growth. Examples of this are shown in the next section, when we consider the spherical case in dimensionalized form.

8 APPLICATION TO THE INNER-CORE GROWTH PROCESS

8.1 The importance of compaction

The inner core grows from the centre of the Earth as the core cools and solid iron precipitates upon the inner-core surface throughout its history. This therefore becomes a good example of sedimentary compaction. An example of 'snow flakes' or dendrites of alloys can be seen from recovered samples of high pressure and temperature experiments, e.g. Kato & Ringwood (1989). However, as noted in the introduction, past work on the inner-core structure has neglected compaction. Apart from such models of the inner core, there have been an increasing number of theoretical works on the structure of the mushy layer and compositional convection occurring there. An analytically derived porosity structure in the presence of convection was obtained by Worster (1991), whose non-linear effects were studied by Amberg & Homsey (1993). Worster (1992) discovered two modes of compositional convection, and its quantitative understanding was undertaken by Emms & Fowler (1994). Further, disequilibrium effects at the mush–liquid interface were incorporated by Worster & Kerr (1994). As with the previous models of the inner core, in all of the above works the solid matrix was assumed immobile, and the process of compaction was neglected for simplicity and consequently excluded from the set of equations considered. The reason for this neglect was probably because compaction did not occur in laboratory experiments such as those of Tait, Jahrling & Jaupart (1992). This neglect is quite serious if one wants to deduce the structure of the inner core, since the spatial and temporary scales of laboratory experiments and those of the inner core differ, and compaction inevitably occurs in the inner core, as we shall show in the calculations in the next section. It is our belief that any theoretical model aiming to simulate the inner core structure must take compaction processes into account. Through such considerations, it becomes possible to interpret and utilize, as well as predict, seismic structure of the inner core. Furthermore, the degree of compaction affects the degree of heat and compositional transport from the inner core to the outer core and determines the boundary condition for outer-core fluid flow. Therefore it is essential to clarify the physics of sedimentary compaction as one of the elementary processes at the inner-core boundary to understand the core dynamics. An analogous phenomenon might have occurred in meteorite parent bodies, since iron meteorites often exhibit the remanences of a solid–fluid com-

posite. It is not certain whether the inner-core growth is occurring through sedimentation (i.e. snow fall) or dendritic growth, but, as explained in Section 2, as far as the compaction process is concerned, the structures formed are irrelevant to the style of growth.

We have focused upon the compaction aspect of this problem while previous authors have paid attention to the thermal and compositional aspects. In the next section, we shall present the inner-core structure determined from compaction alone, and interpret the results based on the results obtained so far. In Section 8.3, we show that compaction is of primary importance, even in the presence of a phase change and convection.

8.2 Numerical results

In the case for the inner core, all three factors discussed in Section 7 are present. On the dimensionalized scale, we shall study the magnitude of mushy layer thickness and residual porosity, as well as other characteristic features (i.e. inverted porosity structure and solitary waves) of the resulting porosity structure.

Let us first make an estimate of the order of magnitude of the mushy-layer thickness and residual porosity. The sedimentation rate at the present inner core is estimated to be $\sim 10^{-12}$ m s^{-1} if the inner core formed in 4×10^9 years at a constant volumetric rate (i.e. ~ 100 m^3 s^{-1}), which is coincidentally about the same order of magnitude as the sedimentation rate of deep sea sediments (i.e. 1 cm kyr^{-1}). Using eq. (76), and typical values for the core as in Table 2 ($\eta_s \sim 10^{16}$ Pa s), we see that the mushy layer thickness becomes very small, of the order of 10 m. High solid viscosity, of the order of 10^{20} Pa s, still makes the mushy layer thickness about 1 km, very small compared to the inner-core radius of 1220 km. We see from this result that compaction is extremely important in determining the porosity structure. However, this does not mean that the inner core contains a negligible amount of liquid. The residual porosity can be sufficiently large, depending on the magnitude of permeability, which we consider to be a function of grain size. Using Fig. 5(d), the relationship between the residual porosity and the sedimentation rate, we see that if the surface permeability is smaller than 10^{-16} m^2, which corresponds to a grain size of the order of 10^{-6} m if we use the permeability formula given by eq. (15), then the residual porosity becomes ~ 0.01, and smaller permeability values mean that the inner core contains an appreciable volume of liquid. Though it again seems to be a mere coincidence, the permeability value which the inner-core porosity structure is sensitive to is similar to the permeability of deep-sea sediments (Table 2).

Let us now proceed on to the numerically calculated inner-core structure and study the structure in more detail. According to our study of the thermal history of the core, the inner core grew proportional to the square root of time (Sumita *et al.* 1995), which means that the volumetric sedimentation rate is proportional to the square root of the inner-core radius. If we assume that the inner core grew to its present size ~ 2500 Myr after its nucleation, which can be constrained from the thermal history and size of the inner core (Sumita *et al.* 1995), we can constrain the sedimentation rate, as a function of inner core radius r, as

$$200(\mathrm{m^3\,s^{-1}})\sqrt{\frac{r(\mathrm{km})}{1220(\mathrm{km})}}.$$

For ease of numerical calculations, we shall use a large solid viscosity of $\eta_s = 8 \times 10^{21}$ Pa s, but this does not affect the porosity structure greatly, because the major parameter is the ratio of the sedimentation rate to Darcy velocity, which is independent of solid viscosity. We shall use $\phi_0 = 0.4$ for the surface porosity value as a typical value of critical melt fraction, but, as has been discussed in Section 5.3, the exact value is unimportant to the magnitude of the mushy-layer thickness and residual porosity. The grain size of particles in the core is uncertain but a study of the entrainment of sediments (Solomatov, Olson & Stevenson 1993) suggests that at core conditions a particle of diameter greater than 3×10^{-8}–10^{-7} m is large enough not to be entrained by the outer-core thermal convection. This gives the minimum possible grain size at core condition.

Fig. 7(a) shows the calculated inner-core growth, and its associated structural evolution, for a surface permeability value of $K_{\phi_0} = 2.7 \times 10^{-17}$ m^2, or a grain size of 3×10^{-7} m. The residual porosity decreases with time, together with the formation of a solitary wave and porosity inverted structure.

Fig. 7(b) shows the permeability dependence of the inner-core porosity structure at the present inner-core size by calculating the evolution after inner-core nucleation. Cases (1) to (3) are those for which $V_0 \gg V_D(K_{\phi_0} \ll 8 \times 10^{-18}$ m$^2)$ and, as has been discussed for the columnar case in Section 5.3, we shall call this the non-stationary state. Although Darcy balance predominates throughout the profile, the deformation term gradually grows in magnitude near the surface with the increase in surface permeability value. Cases (4) to (6) are those for which $V_0 \sim V_D(K_{\phi_0} \sim 8 \times 10^{-18}$ m$^2)$, and deformation balance starts to form near the surface. A mushy layer of the thickness expected from analytical theory (eq. 76) becomes evident, and we shall call this the transitional state between the non-stationary and quasi-stationary states. Cases (7) to (10) are those for $V_0 < V_D(K_{\phi_0} > 8 \times 10^{-18}$ m$^2)$, where deformation balance in the region of the mushy layer is established, and Darcy balance forms in the region of residual porosity. We shall call this the quasi-stationary state, in that the mushy layer has become the thickness expected from theory. Due to the decrease in sedimentation rate with time, the residual porosity decreases upwards around the base of the mushy zone. This results in the formation of an inverted porosity structure, where a low-porosity layer overlies a layer of higher porosity, accompanied by solitary waves behind it as a means of fluid transportation. The former may be seismically observable as an inner core 'crust', and the latter may result in the eruption of fluid blobs that rise up through the outer core and affect geomagnetism (Kobayashi, Abe & Fukao 1993; Moffatt & Loper 1994). When the permeability becomes large as in case (10), it becomes difficult for solitary waves to form, and for even larger permeability values it is concluded that the inner core does not contain an appreciable amount of liquid.

Figs 7(c) and (d) show the solid viscosity dependences for the quasi-stationary and transitionary states. From Fig. 7(c) (quasi-stationary state), we see that the magnitude of the solid viscosity affects the region of deformation balance through the magnitude of the mushy-layer thickness and the wave length of the solitary waves (see eq. 76), but not for the region of Darcy balance, and the residual porosity remains unaffected (see eq. 77). We also see that solitary waves form more easily for the smaller solid viscosity values. From Fig. 7(d) (transitionary state), we see similar effects of the solid viscosity values, [cases (d) and (e) of Fig. 7d]. We can see that the solid viscosity

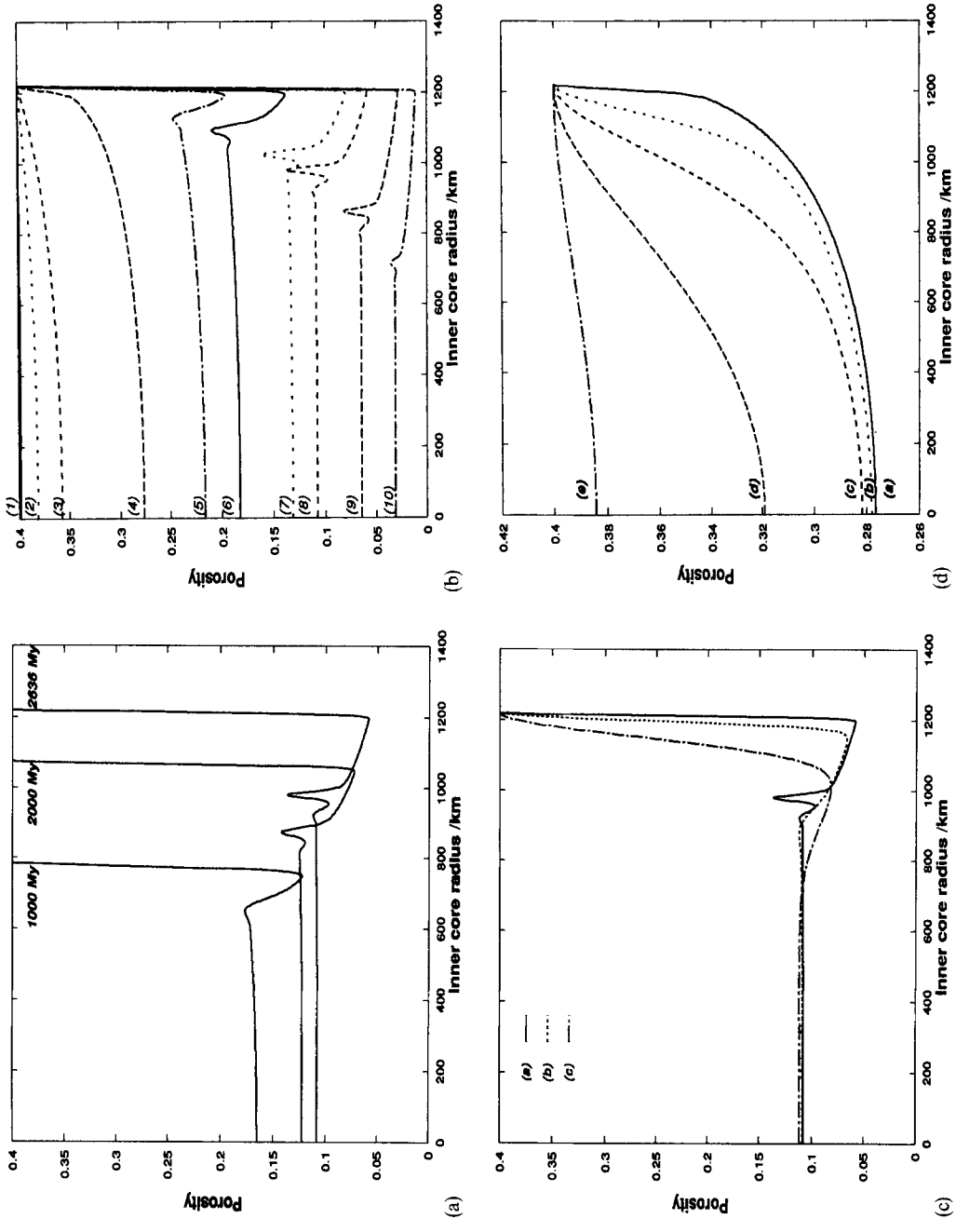

Figure 7. (a) Porosity structure of the inner core. The sedimentation volume is given as a function of inner core radius by $200(\mathrm{m^3\,s^{-1}})\sqrt{r(\mathrm{km})/1220(\mathrm{km})}$, and the calculated porosity profile is at 1000, 2000 and 2636 Myr after inner-core nucleation. The solid viscosity is $\eta_s = 8 \times 10^{21}$ Pa s and the surface permeability value is $K_{\phi_0} = 2.7 \times 10^{-17}\,\mathrm{m^2}$. The surface porosity value is now taken as $\phi_0 = 0.4$. Note the decrease in residual porosity, the formation of an unstable porosity structure, and the appearance of a solitary wave with time. (b) Permeability dependence of the porosity structure of the inner core under the same volumetric sedimentation rate, surface porosity and solid viscosity as in Fig. 7(a). Each line represents the case for different surface permeabilities, K_{ϕ_0}, which is a function of the grain size. (1) 3×10^{-20}, (2) 3×10^{-19}, (3) 7.5×10^{-19}, (4) 3×10^{-18}, (5) 6×10^{-18}, (6) 9×10^{-18}, (7) 1.8×10^{-17}, (8) 2.7×10^{-17}, (9) 7.5×10^{-17}, (10) 3×10^{-16} ($\mathrm{m^2}$). The cases for large surface permeability values take a longer time to form an inner core of the present size (i.e. 1220 km). (c) Solid viscosity dependence of the quasi-stationary porosity structure of the inner core, with boundary conditions the same as those in Fig. 7(a). This figure shows the solid viscosity dependence corresponding to case (8) of Fig. 7(b). Each line is the case for a different solid viscosity, η_s: (a) 8×10^{21} [the same as (8) of Fig. 7b], (b) 8×10^{22}, (c) 8×10^{23}(Pa s). (d) Solid viscosity dependence of the transitional type porosity structure of the inner core with the boundary conditions the same as those in Fig. 7(a). This figure shows the solid viscosity dependence corresponding to case (4) of Fig. 7(b). Each line is the case for a different solid viscosity, η_s: (a) 8×10^{21} [the same as case (4) of Fig. 7b], (b) 8×10^{23}, (c) 8×10^{24}, (d) 8×10^{25}, (e) 8×10^{26}(Pa s). For (a), the mushy layer is thin (~10 km), with compaction balance confined to this layer and Darcy balance below this layer. For (d), the mushy layer is thick (~1000 km) and compaction balance predominates throughout the inner core.

starts to affect the porosity structure in the scale of the inner core only if the solid viscosity becomes larger than about 10^{22} Pa s. However, such a huge viscosity, comparable to, or larger in magnitude than, that of the mantle, seems hardly possible, considering the high homologous temperature of the inner core. Thus it can be concluded that the magnitude of the solid viscosity does not affect the macroscopic porosity structure of the inner core for the reasonable solid viscosity estimate of $\eta_s \ll 10^{22}$ Pa s. If solitary waves do form, however, their shapes and phase velocities would be affected by the solid viscosity, since the wavelength of the solitary wave is about twice the mushy layer thickness. Hence we can conclude that in the Earth's inner core, seismically detectable porosity is due to residual porosity, and the magnitude of the surface permeability governs the porosity structure and is independent of the solid viscosity.

Some inferences about the seismic structure of the inner core can be made, based on the calculated results. Seismic observations show that the Poisson's ratio is anomalously high ($\sim$0.44; Dziewonski & Anderson 1981), and this is often interpreted as being due to partial melting. If we assume that the present inner core contains sufficient liquid to affect seismic waves, we can conclude that the permeability of the inner core is quite small, $< 10^{-16}$ m^2. Considering the textural dependence of permeability given in eq (15), this could be due to small grain size, $a < 1$ μm and/or to a decrease in the connectivity of the fluid phase (an increase in the value of K) by the appearance of the 'swiss cheese' state. We also know the inner-core boundary of the Earth is seismically sharp (Masters & Shearer 1990), and the thin mushy-layer thickness obtained from the discussions above can be its cause, which means that the compaction appears to be very efficient. If this is really the case then, due to the viscous deformation of the solid matrix, the interstitial fluid in the matrix should be in a lens-like form, perpendicular to the radial direction. This could produce a seismic anisotropy different to that observed already (e.g. Shearer 1994) that differs in radial and lateral directions, and could be observed from free oscillations.

It should be noted that the assumption of Newtonian creep, as formulated in eq. (5), can be found to be valid by considering the deformation mechanism. The ratio of the differential pressure between the solid and liquid, ΔP as evaluated in eq. (78), normalized to the solid rigidity $\mu \sim 156.7$ GPa (Dziewonski & Anderson 1981) becomes

$$\frac{\Delta P}{\mu} \sim \frac{\sqrt{\Delta\rho g \eta_s V_0}}{\mu} \sim 3 \times 10^{-8} \sqrt{\left(\frac{\eta_s}{10^{16}(\text{Pa s})}\right)\left(\frac{V_0}{10^{-12}(\text{m s}^{-1})}\right)}. \quad (90)$$

Using the deformation mechanism maps of Frost & Ashby (1982), we see that the solid deforms by diffusion creep, i.e. as a Newtonian viscous fluid, when $\Delta P/\mu < 10^{-5}$, which is consistent with the assumption.

When we focus our attention to the stage of inner-core nucleation, the calculations imply that it was easier for a porous inner core to form, due to a fast sedimentation rate and low gravity. As can be seen from the result of compaction in a sphere, a porosity inversion occurred due to the decrease in the sedimentation rate as the inner core grew, which can be stated as an unavoidable consequence of inner-core growth when the effect of compaction is strong.

8.3 Effects of phase change and convection

Let us discuss the effects that were not included in the present mechanical compaction model, i.e. the effects of phase change and convection. Fowler (1990) addressed the problem of whether thermodynamics or compaction is the governing factor in the coupled problem, and the same problem persists in the case for the inner-core growth process as well as in magma chambers or the magma ocean. The study of the combined result of compaction and thermo-chemical effects is in progress, some of whose results are given in Sumita *et al.* (1995), which shows that in the presence of phase change, but in the absence of convection, its effects are to decrease the porosity further, and the characteristic form of the porosity structure remains basically the same as when only compaction is considered.

As for the effect of convection, from the calculated temperature profile of the inner core, we have already shown that thermal convection is difficult (Sumita *et al.* 1995), but compositional convection driven by the existence of comparatively light-element-rich fluid at deeper parts may occur. One may ask what happens to the porosity structure under the coexistence of compaction and convection. The condition for compositional convection is evaluated by the magnitude of the compositional Rayleigh number in a porous medium

$$Ra_c = \frac{g\Delta\rho_{\text{mush}} K_{\phi_0} H}{\kappa \eta_f}, \quad (91)$$

where H is the mushy layer thickness, $\Delta\rho_{\text{mush}}$ is the density difference of the liquid between the top and bottom of the mushy layer, and κ is the thermal diffusivity. Laboratory experiments and analytical analysis tells us that the critical Rayleigh number is of the order of 10 (Worster 1992; Tait & Jaupart 1992). By assuming an appropriate phase diagram, as in Sumita *et al.* (1995), the case where compositional convection occurs is found to be

$$\{R_{IC}^2 - (R_{IC} - H)^2\} K_{\phi_0} H > 200, \quad (92)$$

where R_{IC} is the inner core radius. When we take $H = 1220$ km, the largest possible value for H, we see that compositional convection occurs for a surface permeability value of larger than 10^{-16} m^2. The permeability range which drastically affects the inner-core porosity structure (Fig. 7b) is smaller than the critical permeability required for mushy-layer compositional convection to occur, so our calculated porosity structures shown in Fig. 7(b) corresponds to the case when compositional convection does not occur. For permeability values larger than this, we have seen that the residual porosity becomes very small, so compositional convection is only possible in the thin mushy layer whose Rayleigh number becomes smaller, making convection more difficult. Further, it can be shown that convective motion cannot prevent the solid matrix from compacting. The magnitude of the shear stress exerted by the convecting fluid upon the solid matrix is of the order of $\eta_f v/a$, where a is the grain size of the matrix, which can be thought of as being the maximum stress that the convective fluid can exert upon the solid matrix. On the other hand, the magnitude of the differential pressure between the solid and the liquid has been evaluated, as in eq. (78). The ratio of the above two quantities is given by

$$\frac{\text{Shear stress by convective flow}}{\text{Differential pressure}}$$

$$\sim 2\times 10^{-5}\left(\frac{v}{10^{-4}(\mathrm{m\,s^{-1}})}\right)\left(\frac{10^{-6}(\mathrm{m})}{a}\right)\sqrt{\frac{10^{16}(\mathrm{Pa\,s})}{\eta_s}} \ll 1. \tag{93}$$

In the above evaluation, we have used the values in Table 2. The value of $v \sim 10^{-4}\,\mathrm{m\,s^{-1}}$ used for fluid velocity is the typical convective velocity of the outer core (Bloxham 1989), and can be taken as the upper limit of the convective velocity in the porous mushy layer. The grain size of $\sim 10^{-6}$ m is the minimum grain size required for compositional convection when we use the permeability formula given in eq. (15), and larger grain sizes only act to enhance compaction. As can be seen from the above evaluation, an extremely fast convective velocity of the order of $v \sim 10\,\mathrm{m\,s^{-1}}$ is required to prevent the solid matrix from compacting, which is hardly possible. Thus we can conclude that, even if compositional convection occurs within the mushy layer due to large permeability, it is impossible for the convective flow to prevent the solid matrix from compacting. This means that the porosity structure is still determined by compaction, and by making the mushy-layer thickness small, and lowering the permeability, compositional convection eventually ceases. A similar conclusion was qualitatively inferred by Sparks *et al.* (1985) from a study of postcumulus processes in magma.

9 CONCLUDING REMARKS

Let us now see what other inferences can be made from this study. In the case of the Earth's core, it is likely that the sedimentation rate is smaller than the Darcy velocity [cases (6) to (10) of Fig. 7b]. However, in smaller planetary bodies, which should have cooled rapidly, it is very probable that the solidifying core was in a highly porous, partially molten state, because of larger sedimentation rates (i.e. $V_0 \gg 10^{-12}\,\mathrm{m\,s^{-1}}$) than those of the Earth's inner core. The presence of troilite patches in iron meteorites (e.g. Buchwald 1975) suggests that partial melts have a 'sponge' or mush texture, where both solid and liquid are linked together in the parent body. It would be intriguing to deduce information from these textures by examining the fraction of the cross-section area of the iron-poor part that occurs as residual porosity. This would enable us to gain more information, such as the size of the parent body, together with the thermal history of the parent body determined from the Widmanstätten pattern. Similarly, for the magma ocean, where solidification proceeded rapidly, the case where sedimentation rate is larger than the Darcy velocity, i.e. the $V_0 > V_D$ case, seems to have been realized (Tonks & Melosh 1990; Solomatov & Stevenson 1993). The results in this paper indicate that one need not consider deformative compaction for the magma ocean at the stage when sedimentation is in progress. This does not mean, however, that differentiation does not occur, since the porosity does decrease from the base by percolative compaction (Fig. 2a).

As a final remark, we would like to stress the extreme importance of compaction on the porosity profile of the inner core, which has hitherto been neglected. Other effects, such as that of phase change and compositional convection, do not greatly affect the porosity structure, and we anticipate that, based on the present work, we can devise a realistic structural model of the inner core.

To summarize, from the study of mechanical sedimentary compaction, the following conclusions were reached.

(1) Mushy layer thickness and residual porosity are characteristic features for sedimentation rates smaller than the Darcy velocity, and are a function of the sedimentation rate, but are only weakly dependent on the magnitude of the surface porosity when sedimentation solid flux is the same. An analytical analysis shows that the evolving porosity profile can be considered to be a half-sided solitary wave.

(2) Decrease in the sedimentation rate as a function of time results in the formation of a low-porosity region at the base of the mushy layer and in the appearance of a solitary wave.

(3) If we consider mechanical compaction only, the porosity structure of the Earth's inner core is governed by the magnitude of the permeability at the inner-core boundary alone, and three regimes are present.

(a) If $V_0 \gg V_D(K_{\phi_0} \ll 8\times 10^{-18}\,\mathrm{m^2})$, a non-stationary porosity profile forms, which shows gradually decreasing porosity with depth. Darcy balance predominates, with a minor contribution from the deformation term.

(b) If $V_0 \sim V_D(K_{\phi_0} \sim 8\times 10^{-18}\,\mathrm{m^2})$, a transitional type between a quasi-stationary and a non-stationary porosity profile forms. Deformation balance becomes evident near the ICB.

(c) If $V_0 < V_D(K_{\phi_0} > 8\times 10^{-18}\,\mathrm{m^2})$, a quasi-stationary profile forms, characterized by two regions: (i) an upper region with a quasi-stationary profile of deformation balance. There is a mushy layer with an inner core 'crust' (a low porosity region) below, accompanied by solitary waves behind; (ii) a lower region with an equi-porosity (residual porosity) profile, which decreases with time. Darcy balance occurs in this region. For $K_{\phi_0} \gg 10^{-16}\,\mathrm{m^2}$, the inner core no longer contains an appreciable amount of liquid.

ACKNOWLEDGMENTS

The authors thank S. Kaneshima for invaluable discussions concerning the seismology of the inner core.

REFERENCES

Amberg, G. & Homsey, G.M., 1993. Nonlinear analysis of buoyant convection in binary solidification with application to channel formation, *J. Fluid Mech.*, **252,** 79–98.

Arzi, A.A., 1978. Critical phenomena in the rheology of partially melted rocks, *Tectonophysics,* **44,** 173–184.

Audet, D.M. & Fowler, A.C., 1992. A mathematical model for compaction in sedimentary basins, *Geophys. J. Int.,* **110,** 577–590.

Barcilon, V. & Richter, F.M., 1986. Nonlinear waves in compacting media, *J. Fluid. Mech.,* **164,** 429–448.

Birch, F., 1964. Density and composition of the mantle and core, *J. geophys. Res.,* **69,** 4377–4388.

Birchwood, R.A. & Turcotte, D.L., 1994. A unified approach to geopressuring, low-permeability zone formation, and secondary porosity generation in sedimentary basins, *J. geophys. Res.,* **99,** 20 051–20 058.

Bloxham, J., 1989. Simple models of fluid flow at the core surface derived from geomagnetic field models, *Geophys. J. Int.,* **99,** 173–182.

Buchwald, V.F., 1975. *Handbook of iron meteorites,* Univ. California Press, California, CA.

Dziewonski, A.M. & Anderson, D.L., 1981. Preliminary Reference Earth Model, *Phys. Earth planet. Inter.,* **25,** 297–356.

Emms, P.W. & Fowler, A.C., 1994. Compositional convection in the solidification of binary alloys, *J. Fluid Mech.,* **262,** 111–139.

Fearn, D.R., Loper, D.E. & Roberts, P.H., 1981. Structure of the Earth's inner core, *Nature,* **292,** 232–233.

Fowler, A.C., 1990. A compaction model for melt transport in the Earth's asthenosphere, in *Magma Transport and Storage,* pp. 3–32, ed. Ryan, M.P., John Wiley and Sons Ltd, Chichester.
Frost, H.J. & Ashby, M.F., 1982. *Deformation mechanism maps,* Pergamon Press, Oxford.
Gibson, R.E., 1958. The progess of consolidation in a clay layer increasing in thickness with time, *Geotechnique,* **8,** 171–182.
Gow, A.J. & Ramseier, R.O., 1963. Age hardening of snow at the south pole, *J. Glaciology,* **4,** 521–536.
Haq, B.U. *et al.,* 1990. *Proc ODP Init. Repts.,* **122,** College Station, TX (Ocean Drilling Program).
Ida, Y. & Kumazawa, M., 1986. Ascent of magma in a deformable vent, *J. geophys. Res.,* **91,** 9297–9301.
Irvine, T.N., 1980. Magmatic infiltration metasomatism, double diffusive fractional crystallization, and adcumulus growth in the Muskox intrusion and other layered intrusions, in *The physics of magmatic processes,* pp. 325–383, ed. Hargraves, R.B. Princeton University Press, Princeton.
Jacobs, J.A., 1953. The Earth's inner core, *Nature,* **172,** 297–298.
Kato, T. & Ringwood, A.E., 1989. Melting relationships in the system Fe–FeO at high pressures: implications for the composition and formation of the Earth's core, *Phys. Chem. Miner.,* **16,** 524–538.
Kobayashi, S., Abe, Y. & Fukao, Y., 1993. Fluid motion induced by gravitational differentiation of immiscible two phases: Basic equations and linear analyses, *J. Geomagn. Geoelect.,* **45,** 1467–1480.
Loper, D.E., 1983. Structure of the inner core boundary, *Geophys. astrophys. Fluid Dyn.,* **22,** 139–155.
Loper, D.E. & Fearn, D.R., 1983. A seismic model of a partially molten inner core, *J. geophys. Res.,* **88,** 1235–1242.
Masters, T.G. & Shearer P.M., 1990. Summary of seismological constraints on the structure of the Earth's core, *J. geophys. Res.,* **95,** 21 691–21 695.
McKenzie, D.P., 1984. The generation and compaction of partially molten rock, *J. Petrol.,* **25,** 713–765.
McKenzie, D.P., 1987. Compaction of igneous and sedimentary rocks, *J. geol. Soc., Lond.,* **144,** 299–307.
Moffatt, H.K. & Loper, D.E., 1994. The magnetostrophic rise of a buoyant parcel in the Earth's core, *Geophys. J. Int.,* **117,** 394–402.
Ribe, N.M., 1985. The deformation and compaction of partial molten zones, *Geophys. J. R. astr. Soc.,* **83,** 487–501.
Richter, F.M., 1986. Simple models for trace element fractionation during melt segregation, *Earth planet. Sci. Lett.,* **77,** 333–344.
Richter, F.M. & McKenzie, D., 1984. Dynamical models for melt segregation from a deformable matrix, *J. Geol.,* **92,** 729–740.
Safronov, V.S., 1978. The heating of the earth during its formation, *Icarus,* **33,** 3–12.
Scott, D.R. & Stevenson, D.J., 1984. Magma Solitons, *Geophys. Res. Lett.,* **11,** 1161–1164.
Scott, D.R. & Stevenson, D.J., 1986. Magma ascent by porous flow, *J. geophys. Res.,* **91,** 9283–9296.
Shearer, P.M., 1994. Constraints in inner core anisotropy from PKP(DF) travel times, *J. geophys. Res.,* **99,** 19 647–19 659.
Shirley, D.N., 1986. Compaction of igneous cumulates, *J. Geol.,* **94,** 795–809.
Solomatov, V.S. & Stevenson, D.J., 1993. Nonfractional crystallization of a terrestrial magma ocean, *J. geophys. Res.,* **98,** 5391–5406.
Solomatov, V.S., Olson, P. & Stevenson, D.J., 1993. Entrainment from bed of particles by thermal convection, *Earth. planet. Sci. Lett.,* **120,** 387–393.
Sparks, R.S.J., Huppert, H.E., Kerr, R.C., McKenzie, D.P. & Tait, S.R., 1985. Postcumulus processes in layered intrusions, *Geol. Mag.,* **122,** 555–568.
Stevenson, D.J., 1990. Fluid dynamics of core formation, in *Origin of the Earth,* pp. 231–249, eds Newsom, H.E. & Jones, J.H., Oxford Univ. Press, New York.
Sumita, I., Yoshida, S., Hamano, Y. & Kumazawa, M., 1995. A model for the structural evolution of the Earth's core and its relation to the observations, in *The Earth's Central Part: Its Structure and Dynamics,* pp. 231–261, ed. Yukutake, T., Terra Scientific Publishing Company, Tokyo.
Tait, S. & Jaupart, C., 1992. Compositional convection in a reactive crystalline mush and evolution of porosity, *J. geophys. Res.,* **97,** 6735–6756.
Tait, S., Jahrling, K. & Jaupart, C., 1992. The planform of compositional convection and chimney formation in a mushy layer, *Nature,* **359,** 406–408.
Tonks, W.B. & Melosh, H.J., 1990. The physics of crystal settling and suspension in a turbulent magma ocean, in *Origin of the Earth,* pp. 151–174, eds Newsom, H.E. & Jones, J.H., Oxford Univ. Press, New York.
Toramaru, A. & Fujii, N., 1986. Connectivity of melt phase in a partially molten peridotite, *J. geophys. Res.,* **91,** 9239–9252.
Wangen, M., 1992. Pressure and temperature evolution in sedimentary basins, *Geophys. J. Int.,* **110,** 601–613.
Whitehead, J.A. & Helfrich, K.R., 1986. The Koreteweg–deVries equation from laboratory conduit and magma migration equations, *Geophys. Res. Lett.,* **13,** 545–546.
Worster, M.G., 1991. Natural convection in a mushy layer, *J. Fluid Mech.,* **224,** 335–359.
Worster, M.G., 1992. Instabilities of the liquid and mushy regions during solidification of alloys, *J. Fluid Mech.,* **237,** 649–669.
Worster, M.G. & Kerr, R.C., 1994. The transient behaviour of alloys solidified from below prior to the formation of chimneys, *J. Fluid Mech.,* **269,** 23–44.
Yoshida, S., Sumita, I. & Kumazawa, M., 1996. Growth model of the inner core coupled with the outer core dynamics and the resulting elastic anisotropy, *J. geophys. Res.* (submitted).

APPENDIX A: DERIVATION OF EFFECTIVE VISCOSITY

Let us assume a situation where pores of radius R are uniformly distributed throughout a viscous medium. We shall describe the overall behaviour of the medium by studying one of the pores and neglecting the interaction between pores.

First, we derive the flow of the solid matrix around a single pore, driven by a pressure difference between the solid and the fluid, $P_s - P_f$. We assume that the deformation is governed by the solid alone, and that the fluid in the pores flows in and out of them freely. We assume that the velocity is described by the potential Φ in the matrix,

$$\mathbf{V} = \nabla\Phi. \tag{A1}$$

We assume incompressibility:

$$\nabla \cdot \mathbf{V} = \nabla \cdot \nabla\Phi = 0, \tag{A2}$$

and a radially symmetric potential:

$$\Phi = \frac{m}{r}. \tag{A3}$$

We set boundary condition at $r = R$ as $\partial\Phi/\partial r = \dot{R}$, to obtain

$$\Phi = -\frac{R^2\dot{R}}{r}, \tag{A4}$$

$$V = \dot{R}\left(\frac{R}{r}\right)^2. \tag{A5}$$

We assume that the pressure gradient balances the viscous force in the solid,

$$\nabla P = \eta_s \Delta \mathbf{V}$$
$$= \eta_s \,\mathrm{grad}\, \Delta\Phi. \tag{A6}$$

Substitution of eq. (A5) into eq. (A6) gives

$$\nabla P_s = 0 \tag{A7}$$

Therefore the pressure in the solid is constant. The pressure difference between the fluid and the solid is given by the stress boundary condition at the interface:

$$P_s - P_f = 2\eta_s \frac{\partial V}{\partial r} = -4\eta_s \frac{\dot{R}}{R}. \tag{A8}$$

Next, we apply the above result to the property of a bulk system, neglecting the interaction between the pores. If the number of pores per unit volume is n, the porosity becomes

$$\phi = \frac{4}{3}\pi R^3 n, \tag{A9}$$

which leads to

$$\frac{\dot{\phi}}{\phi} = 3\frac{\dot{R}}{R}. \tag{A10}$$

Using eq. (A8) we get

$$\frac{\dot{\phi}}{\phi} = -\frac{3}{4\eta_s}(P_s - P_f), \tag{A11}$$

which is transformed to

$$\frac{1}{\phi}\frac{D_V \phi}{Dt} = -\frac{3}{4\eta_s}(P_s - P_f). \tag{A12}$$

Hence,

$$\begin{aligned} P_s - P_f &= -\frac{4}{3}\eta_s \frac{1}{\phi}\left(\frac{\partial \phi}{\partial t} + \mathbf{V}\cdot\nabla\phi\right) \\ &= -\frac{4}{3}\frac{1-\phi}{\phi}\eta_s \nabla\cdot\mathbf{V}. \end{aligned} \tag{A13}$$

We hereby obtain the expression for effective viscosity as

$$\eta_\phi^* = \frac{4}{3}\frac{1-\phi}{\phi}\eta_s. \tag{A14}$$

APPENDIX B: DERIVATION OF THE KdV EQUATION

The basic equations form the KdV equation when residual porosity is large, namely when the amplitude of the porosity profile is small. We can derive the KdV equation in the same way as that of Whitehead & Helfrich (1986).

First, we expand the basic equations to the quadratic term of non-linearity. We take the basic state of ψ and $\hat{V}$ as

$$\psi = \psi_1, \tag{B1}$$

$$\hat{V} = -\left(\frac{1-\psi_1}{1-\psi_0}\right)^3 \frac{\psi_0}{\psi_1}. \tag{B2}$$

By expanding eqs (24) and (31) to the second order, we obtain

$$\frac{\partial \psi'}{\partial \hat{t}} = \left(\frac{1-\psi_1}{1-\psi_0}\right)^3 \frac{\psi_0}{\psi_1}\frac{\partial \psi'}{\partial \hat{z}} - \psi_1 \frac{\partial V'}{\partial \hat{z}} - V'\frac{\partial V'}{\partial \hat{z}} - V'\frac{\partial \psi'}{\partial \hat{z}} - \psi'\frac{\partial V'}{\partial \hat{z}}, \tag{B3}$$

$$\begin{aligned} V' = {} & \left(\frac{1-\psi_1}{1-\psi_0}\right)^3 \frac{\psi_0(1+2\psi_1)}{\psi_1(1-\psi_1)}\psi' \\ & - \left(\frac{1-\psi_1}{1-\psi_0}\right)^3 \frac{\psi_0(1+\psi_1+\psi_1^2)}{\psi_1^3(1-\psi_1)^2}\psi'^2 \\ & + \left(\frac{1-\psi_1}{1-\psi_0}\right)^2 \frac{\partial^2 V'}{\partial \hat{z}^2} + \left(\frac{1-\psi_1}{1-\psi_0}\right)^2 \frac{2-\psi_1}{\psi_1(1-\psi_1)}\frac{\partial \psi'}{\partial \hat{z}}\frac{\partial V'}{\partial \hat{z}}. \end{aligned} \tag{B4}$$

We make the Gardner–Morikawa transformation as follows, to new variables ζ and τ. The new coordinates move at a velocity c_0 relative to the original coordinates

$$\zeta = \varepsilon^{1/2}(\hat{z} - c_0 \hat{t}), \tag{B5}$$

$$\tau = \varepsilon^{3/2} c_0 \frac{1+2\psi_1}{3\psi_1}\left(\frac{1-\psi_1}{1-\psi_0}\right)^2 \hat{t}. \tag{B6}$$

Here, c_0 is the long-wavelength limit of the linear wave given by eq. (39), $c_0 = 3\phi_1^2(1-\phi_0)/\phi_0$, and ε is the factor for perturbative ordering. The factor appearing in eq. (B5) is introduced in accordance with the coefficient of k^2 in the dispersion relation in eq. (38):

$$\frac{\partial}{\partial \hat{z}} = \varepsilon^{1/2}\frac{\partial}{\partial \zeta}, \tag{B7}$$

$$\frac{\partial}{\partial \hat{t}} = -\varepsilon^{1/2} c_0 \frac{\partial}{\partial \zeta} + \varepsilon^{1/2} c_0 \frac{\partial}{\partial \zeta} + \varepsilon^{3/2} c_0 \frac{1+2\psi_1}{3\psi_1}\left(\frac{1-\psi_1}{1-\psi_0}\right)^2 \frac{\partial}{\partial \tau}. \tag{B8}$$

Let us expand the variables as follows:

$$\psi' = \varepsilon\psi', \tag{B9}$$

$$V' = \varepsilon(V'^{(0)} + \varepsilon V'^{(1)} + \varepsilon^2 V'^{(2)} + \cdots). \tag{B10}$$

Here, the superscripts represent the order of expansion. To the zeroth order, eq. (B4) becomes

$$V'^{(0)} = \left(\frac{1-\psi_1}{1-\psi_0}\right)^3 \frac{\psi_0(1+2\psi_1)}{\psi_1^2(1-\psi_1)}\psi'. \tag{B11}$$

The first-order parts of eqs (B3) and (B4) become

$$\frac{(1+2\psi_1)\psi_0}{\psi_1(1-\psi_1)}\left(\frac{1-\psi_1}{1-\psi_0}\right)^5 \frac{\partial \psi'}{\partial \tau} = -\psi_1 \frac{\partial V'^{(1)}}{\partial \zeta} - V'^{(0)}\frac{\partial \psi'}{\partial \zeta} - \psi'\frac{\partial V'^{(0)}}{\partial \zeta} \tag{B12}$$

$$V'^{(1)} = -\left(\frac{1-\psi_1}{1-\psi_0}\right)^3 \frac{\psi_0(1+\psi_1+\psi_1^2)}{\psi_1^3(1-\psi_1)^2}\psi'^{(2)} + \left(\frac{1-\psi_1}{1-\psi_0}\right)^2 \frac{\partial^2 V'^{(0)}}{\partial \zeta^2} \tag{B13}$$

Substituting eq. (B11) into (B12) and (B13), we obtain

$$\frac{\partial \psi'}{\partial \tau} - 2\left(\frac{1-\psi_0}{1-\psi_1}\right)^2 \frac{1+2\psi_1^3}{\psi_1(1-\psi_1)(1+2\psi_1)}\psi'\frac{\partial \psi'}{\partial \zeta} + \frac{\partial^3 \psi'}{\partial \zeta^3} = 0. \tag{B14}$$

If we define the new variable χ as

$$\chi = -\frac{1}{3}\left(\frac{1-\psi_0}{1-\psi_1}\right)^2 \frac{1+2\psi_1^3}{\psi_1(1-\psi_1)(1+2\psi_1)}\psi', \tag{B15}$$

we obtain the KdV equation

$$\frac{\partial \chi}{\partial \tau} + 6\chi\frac{\partial \chi}{\partial \zeta} + \frac{\partial^3 \chi}{\partial \chi^3} = 0. \tag{B16}$$